

Modeling of Geophysical Flows – Analysis of Models and Modeling Assumptions Using UQ

Ali Akhavan Safaei¹, Andrea Bevilacqua², Abani K. Patra^{1,3}, and E. Bruce Pitman⁴

¹*Dept. of Mech. and Aero. Eng., University at Buffalo, Buffalo NY 14260*

²*Dept. of Geology, University at Buffalo, Buffalo NY 14260*

³*Comp. Data Science and Eng., University at Buffalo, Buffalo NY 14260*

⁴*Dept. of Materials Design and Innovation, University at Buffalo, NY, 14260*

{abani,aliakhav,abevilac}@buffalo.edu

Abstract

Dense large scale granular avalanches are a complex class of flows with physics that has often been poorly captured by models that are computationally tractable. Sparsity of actual flow data (usually only a posteriori deposit information is available) and large uncertainty in the mechanisms of initiation and flow propagation make the modeling task challenging and a subject of much continuing interest. Models that appear to represent the physics well in certain flows turn out to be poorly behaved in others due to intrinsic mathematical or numerical issues. Nevertheless, given the large implications on life and property many models with different modeling assumptions have been proposed.

While, inverse problems can shed some light on parameter choices it is difficult to make firm judgements on the validity or appropriateness of any single or set of modeling assumptions for a particular target flow or potential flows that needs to be modeled for predictive use in hazard analysis. We will present here an uncertainty quantification based approach to carefully, analyze the effect of modeling assumptions on quantities of interest in simulations based on three established models (Mohr-Coulomb, Pouliquen-Forsterre and Voellmy-Salm) and thereby derive a model (from a set of modeling assumptions) suitable for use in a particular context. We also illustrate that a simpler though more restrictive approach is to use a Bayesian modeling average approach based on the limited data to combine the outcomes of different models. **REAL DATA?? NOTION OF CONTRIBUTION OF DIFFERENT MECHANISMS OR MODEL ELEMENTS??**

1 Geophysical Flows and Review of Models – Ali

1.1 An Overview of Geophysical Flow Types - Ali

The term “geophysical flow” describes a broad class of flows that covers small mudflows and rockfalls, debris flows, pyroclastic density currents (including pumice and ash and block and ash flows), lava, and dry volcanic debris avalanches. Particles in block and ash flows, debris avalanches, and debris flows typically range from centimeters to meters in size. These flows are sometimes tens of kilometers in length and may travel at speeds as fast as hundreds of meters per second. Their deposits can be as much as 100 meters deep and kilometers long. In other words, there is no single universal description of a “typical” geophysical mass flow, even if we restrict ourselves to those flows occurring at a single volcano. Different types of flows are the results of different types of mechanisms/processes and so different types of flows will have significantly different physical characteristics. For the sake of clarification, let us consider three different types of events that are *pyroclastic pumice and ash flow* (resulting from a column collapse), *pyroclastic block and ash flow* (resulting from a dome collapse) an *volcanic debris avalanche*.

Make Less Volcano specific??

A column collapse pyroclastic flow is formed from a vertically-ejected eruption column. Instead of rising in the eruption plume, denser than air material collapses back to the ground and begins to flow as a gravity current. The kinetic energy of the material that lands on the upper slopes of the volcano is therefore redirected into downslope motion. These types of flow involve ash and low density pumiceous material, formed by vesiculation and fragmentation of gas-rich magmas in the volcanic conduit during the explosions. In a column collapse, during the horizontal component of flow, ambient air is entrained into the flow and heated. The flows therefore involve a mixture of hot gas, ash, and small pumice clasts (a few [cm] to 0.5 [m]). This extremely hot mixture can have initial downslope speeds in the range of 30 – 80 meters per second. The volume of material involved in such a flow is roughly constrained to the volume of the plug and upper conduit (for short-lived explosive eruptions) and therefore will most likely be in the range $10^4 – 10^6$ [m³].

A dome collapse occurs when there is a significant amount of (recently extruded) viscous lava piled up in an unstable configuration around a vent. Further extrusion and/or external forces such as intense rainfall cause the still hot dome of viscous lava to collapse, disintegrate, and avalanche downhill. The hot, dense blocks in this “block and ash” flow will typically range from centimeters to a few meters in size. The matrix is composed of fine ash from the comminuted blocks. The amount of material involved in these collapses is constrained by the size of the newly extruded and still hot dome but usually involves volumes in the range $10^4 – 10^8$ [m³].

A debris avalanche is the failure of a major part of an established volcanic edifice. These usually involve predominantly cold and mechanically weakened rocks as well as large volumes, up to tens of cubic kilometers. The triggering mechanism can be internal (such as the intrusion of new magma and pressurization) or external (such as seismic acceleration, rainfall, etc.). As such, the material involved in these events can be a mixture of fresh magmatic components as well as ancient hydrothermally weakened rocks. The material volume is usually in the range of $10^4 – 3 \times 10^{10}$ [m³]. These types of flows are distinguished in that they involve large parts of the edifice that are not thoroughly broken up, i.e. some particles can be up to hundreds of meters or even kilometers in diameter.

1.2 Modeling Assumptions - Ali

As a matter of fact, a very crucial feature of a sophisticated model for geophysical mass flows is that it is based on *physical reasoning* and *rigorous mathematical foundations*. Subsequently, several simplifying, but nevertheless realistic, assumptions were made that streamlined the mathematical formulation. They as follows:

1. The moving mass was assumed to be *volume preserving*. Since the dynamics define the motion, assuming volume preserving is an adequate approximation.
2. Geophysical mass flows are mostly assumed to be *free surface* flows consist of granular material (i.e. a large collection of discrete particles, frequently with interstitial fluid, and whatever else that get caught in the flow path). In general, the “typical particle” is small compared to the depth and length of the flowing mass and makes it reasonable to model the flowing material as a continuum which implies that the thickness of sliding and deforming body extends over several particle diameters.

Therefore, we can consider an “equivalent flowing material” whose rheological properties are chosen to approximate the bulk behavior that is expected of an actual mass flow; however, the properties of this “equivalent material” may not correspond to those of any component of the actual mass flow.

3. According to the *geometries* of geophysical mass flows, numerous models make the *shallowness* approximation for their numerical simulation. In this approximation, the flow depth is assumed to be at least an order of magnitude less than the characteristic length of the flowing material.
4. The shear stresses lateral to the main flow direction can be neglected.
5. The body of mass is supposed to be in *isothermal* state or, if not, thermal effects can be ignored.
6. The flowing mass is assumed to be consisted of an *incompressible* granular continuum material. This means that we are allowed to ignore variations of density due to the void ratio (density preserving assumption).
7. Motion of the bulk of mass consists of “shearing within the deforming mass” and “sliding along the basal surface”. However, based on the observations, the shearing deformation commonly takes place within a very small boundary layer, so that it is justified to collapse this boundary layer to zero thickness and to combine the sliding and shearing velocity to a single sliding law with a somewhat larger modelled *sliding velocity*. This then effectively means that variations of the material velocities across the flow depth may be ignored and *depth-averaged* equations may be employed ([Savage and Hutter, 1989](#); [Hutter et al., 1993](#)). Details on the integration of continuum models for shallow free surface flows can be studied in ([Pudasaini and Hutter, 2007](#)).
8. The shallowness assumption gives a *hydrostatic* expression for the normal pressure in the direction perpendicular to the basal surface. Moreover, the downslope and cross-slope pressure components are assumed to be varying linearly with the normal pressure component through the flow depth. The coefficient could either be defined based on the rheology model or be constant ([Savage and Hutter, 1989](#); [Bartelt et al., 1999](#); [Iverson and Denlinger, 2001](#); [Denlinger and Iverson, 2001](#)).

1.3 Governing Equations and Boundary Conditions - Ali

Starting with the basic conservation of mass and momentum for an incompressible medium, we can describe the motion of an avalanching mass:

$$\begin{aligned} \nabla \cdot \underline{\mathbf{u}} &= 0, \\ \frac{\partial}{\partial t}(\rho \underline{\mathbf{u}}) + \nabla \cdot (\rho \underline{\mathbf{u}} \otimes \underline{\mathbf{u}}) &= \nabla \cdot \underline{\underline{\mathbf{T}}} + \rho \underline{\mathbf{g}}, \end{aligned} \quad (1)$$

Where $\underline{\mathbf{u}} = [u, v, w]^T$, is the material velocity vector, ρ is its constant density, $\underline{\underline{\mathbf{T}}}$ is the *Cauchy* stress tensor, and $\underline{\mathbf{g}}$ is the gravity vector. Based on the material rheology we choose, the Cauchy stress tensor, $\underline{\underline{\mathbf{T}}}$, is defined differently ([Freundt and Bursik, 1998](#)). Defining the free and basal surface interfaces respectively as follows,

$$\begin{aligned} F^s(x, y, t) &= s(x, y, t) - z, \\ F^b(x, y, t) &= b(x, y, t) - z, \end{aligned} \quad (2)$$

Therefore, one can impose the *kinematic boundary conditions* at free and basal surface interfaces:

$$\frac{\partial F^s}{\partial t} + \underline{\mathbf{u}} \cdot \nabla F^s = 0, \quad \text{at } F^s(x, y, t) = 0 \quad (3)$$

$$\frac{\partial F^b}{\partial t} + \underline{\mathbf{u}} \cdot \nabla F^b = 0, \quad \text{at } F^b(x, y, t) = 0 \quad (4)$$

According to the 2nd and 7th assumptions, we may also impose the traction-free boundary condition at the free surface, while a *Coulomb dry-friction* sliding law at the interface between the granular flow and the basal surface is imposed:

$$\underline{\underline{\mathbf{T}}}^s \underline{\mathbf{n}}^s = \underline{\underline{\mathbf{0}}}, \quad \text{at } F^s(x, y, t) = 0 \quad (5)$$

$$\underline{\mathbf{T}}^b \underline{n}^b - \underline{n}^b (\underline{n}^b \cdot \underline{\mathbf{T}}^b \underline{n}^b) = \frac{\underline{\mathbf{u}}^b}{\|\underline{\mathbf{u}}^b\|} (\underline{n}^b \cdot \underline{\mathbf{T}}^b \underline{n}^b) \mu_{\text{Bed}}, \quad \text{at } F^b(x, y, t) = 0 \quad (6)$$

where μ_{Bed} is the basal friction coefficient and the basal and surface unit normals are:

$$\underline{n}^b = \frac{\nabla F^b}{\|\nabla F^b\|}, \quad \underline{n}^s = \frac{\nabla F^s}{\|\nabla F^s\|}. \quad (7)$$

It is worth mentioning that $\underline{\mathbf{T}} \underline{n}$ is a resisting traction, while $\underline{n} \cdot \underline{\mathbf{T}} \underline{n}$ is the normal pressure and $\underline{n} \cdot \underline{\mathbf{T}} - \underline{n}(\underline{n} \cdot \underline{\mathbf{T}} \underline{n})$ is the resulting shear traction. Considering Equation (6), Coulomb dry-friction sliding law expresses that the magnitude of the basal shear stress is equal to the normal basal pressure multiplied by the basal friction coefficient, μ_{Bed} . Furthermore, Equation (6) is stating that the shear traction is assumed to point in the opposite direction to the basal velocity, $\underline{\mathbf{u}}^b$ (resisting shear traction) which also implicitly assumes that $\underline{\mathbf{u}}^b \cdot \underline{n}^b = 0$ when we also consider the basal kinematic boundary condition.

1.4 Models

2 UQ Process - Andrea

The key purpose of this study is to present a procedure for the improved exploration and quantitative comparison of physical models and their assumptions through the collection of full statistical data. Models are not black boxes, behind each physical model there are different physical assumptions, and therefore it would be more appropriate to look at those instead than at the entire model results. Our statistical approach enables a first step towards a data driven selection of the best modeling assumptions to use.

In particular, a good forecasting capability in the context of mass flows requires the careful selection of the pair $(M(A), P(M(A)))$, where A is a set of assumptions, $M(A)$ is the model which combines those assumptions, and $P(M)$ is a probability distribution in the parameter space of M . An assumption is a quite general concept - for example it can be a specific equation for the internal stress, the implementation of bed curvature effects, of active-passive material stretching, or the use of a specific correction on the pressure effects, etc... Assumptions are what makes the models being different, and each model may be seen as the combined result of a set of assumptions. Sometimes a good model contains a useless assumption that may be removed, sometimes a good assumption should be implemented inside a different model - those are usually considered as subjective choices, not data driven. Moreover, the correct assumptions may change through time, making the analysis more difficult.

It is worth mentioning that whereas the support of $P(M)$ can be restricted to a single point in case an optimization procedure is performed for the reconstruction of a particular flow, this is not possible if we are interested in the general predictive capabilities of the model, i.e. what is desired in probabilistic hazard assessment. In this study we will always assume $P(M) \sim \bigotimes_{i=1}^{N_M} \text{Unif}(a_{i,M}, b_{i,M})$, where N_M is the number of parameters of M . These parameter ranges will not be selected under the influence of a particular observation, but we will try to use the information gathered in literature about the physical meaning of those values.

In general, the simulation algorithms can be classified as:

(1) INPUT VARIABLES \rightarrow (2) DYNAMICAL QUANTITIES \rightarrow (3) OBSERVABLE OUTPUTS

The input variables can include: volume, rheology coefficients, initiation site and geometry, digital elevation map. We will focus on the former two of those, the volume of the pile and the rheology, which constitute our parameter space in all the case studies. The dynamical quantities are directly related to the force terms in the Newton Equations that rule the simulation, they include: driving and dissipative stresses and powers. The terms of the equations are hidden to the observation, but they directly depend on the parameters, and represent a fundamental link between the parameters and the observable outputs. Moreover, the models share some of those terms while change others, and this enables a detailed comparison of the real physics below the curtain. Finally, the observable outputs include: flow height, inundated area, flow velocity and acceleration. In the sequel (2) and (3) are also called quantities of interest (QoI).

Another level of complexity can be achieved choosing the degree of integration of (2) and (3) in the previous scheme:

- (A) LOCAL MEASUREMENTS
- (B) SPATIAL AVERAGES
- (C) TEMPORAL AVERAGES
- (D) SPATIO-TEMPORAL (FULL) AVERAGES

In particular, all the dynamical quantities, and most of the observable outputs, have a local meaning. They are calculated on the elements of the numerical mesh created by the code. Moreover, all those quantities are time dependent. Differences in time and location enable to constrain the changes in flow regime. Those are really important because if the flow behavior is radically different, then the significance and effects of the assumptions may also change.

A first approach to look at the data is to choose a reasonable design of spatial locations and to calculate the graph of the quantities as a function of time. A second approach is to make the spatial integral of those quantities and calculate their temporal graph - this integration can be done with respect to the basal area, e.g. for the stresses and related powers, or with respect to the flow volume, e.g. velocity and acceleration. A third possible approach requires to make the integrals through time at each designed spatial site, a fourth approach the full integral in space-time.

In general, for each QoI and degree of integration, during a Monte Carlo simulation we sample the input variables and obtain a family of temporal graphs in (A), (B), and numeric values in (C), (D). These results are statistically summarized - plotting their expectation, their standard deviation, their 5th and 95 percentiles. Their correlation structure is also explored, presenting the plots of the Pearson coefficients of the most interesting pairs of quantities in (1), (2), (3). In the following, we will detail the considered input variables and quantities of interest for each of our cases study.

Our sampling technique of the input variables is based on the Latin Hypercube Sampling (LHS) idea, and in particular, on the improved space-filling properties of the orthogonal array-based Latin Hypercubes (see Appendix A). The LHS is performed over $[0, 1]^3$ for the MC and VS input parameters, and $[0, 1]^4$ for PF input parameters. Those samples are homothetically transformed to fill the required intervals.

2.1 Definition and consistency of the Input parameters

In general, the three rheologies considered in this study, MC, PF, and VS, have different parameters, but in all them it is defined a basal friction stress F . That is $F = \tan(\phi_{bed})$ in MC, $F = \tan(\phi_2)$ for $Fr \gg h$ in PF, $F = \mu$ in VS. We use those relations to define parameter spaces which produce reasonably consistent ranges of basal frictions. In the following sections, we start defining a range for ϕ_{bed} of MC, specific of the scenario and obtained from the more rich literature of that rheology, then we impose a consistent range for the related parameters of PF and VS, and leave the other parameters unchanged. In particular:

MC

$\phi_{bed} \in [a, b]$, depending on the case study.

$\phi_{int} - \phi_{bed} = \Delta\phi \in [2, 10]$, following [Dalbey et al. \(2008\)](#), but 25% enlargement on the higher side of the uncertainty range.

PF

$\phi_2 = \phi_{bed}$, but with ~20% enlargement on the higher side of the uncertainty range.

$\phi_2 - \phi_1 = \Delta\phi_{12} \in [5, 15]$ ([Gray and Edwards \(2014\)](#) used 9 degrees, [Barker et al. \(2015\)](#) 11 degrees).

$\beta \in [0.1, 0.85]$ ([Gray and Edwards \(2014\)](#) assumed $\beta = 0.14$, [Forterre and Pouliquen \(2003\)](#) $\beta = 0.65$)
 $L = 10^{-3}$, $\phi_3 = 35$ ([Gray and Edwards, 2014](#)) due to their reduced sensitivity (see Appendix B).

VS

$\mu = \tan(\phi_{bed})$, with ~20% enlargement of the uncertainty range.

$\log(\xi) \in [1.7, 4] = \log[50, 10^4]$, i.e. in this case the uniform sampling is accomplished in log-scale.

3 QoIs and Data Collected

3.1 Flow down an inclined plane, and a change in slope to a flat plane

The parameter ranges adopted in this case study are:

MC - $\phi_{bed} \in [15, 30]$ (Dalbey et al., 2008), $\Delta\phi \in [2, 10]$.

PF - $\phi_2 \in [15, 35]$, $\Delta\phi_{12} \in [5, 15]$, $\beta \in [0.1, 0.85]$, $L = 10^{-3}$, $\phi_3 = \phi_1 + 1$.

VS - $\mu \in [0.2, 0.7]$, $\log(\xi) \in [1.7, 4]$.

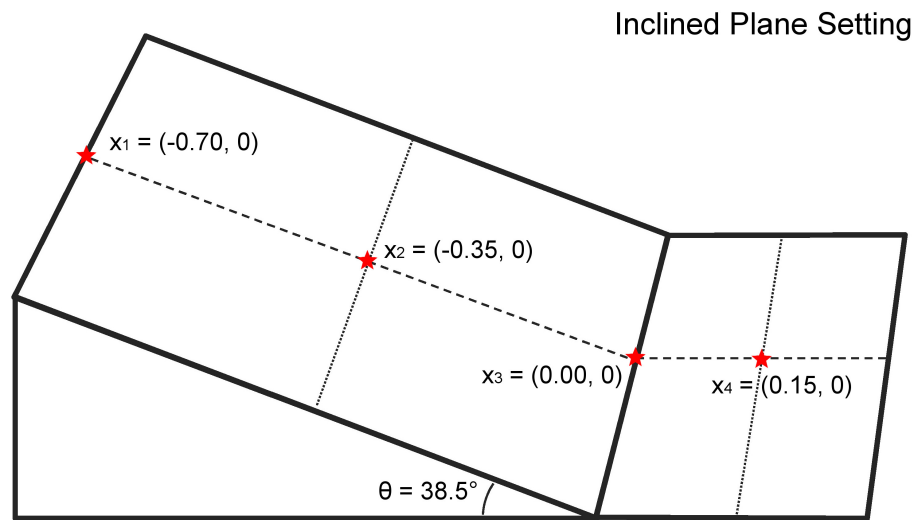
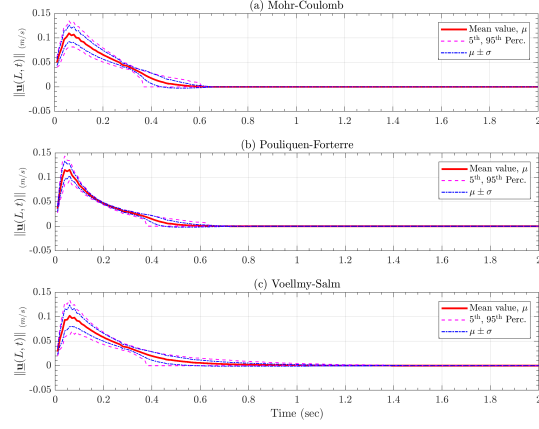
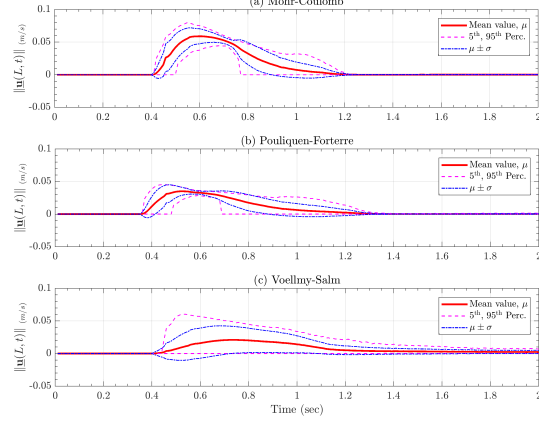


Figure 1: Inclined plane description, including local samples sites (red stars).

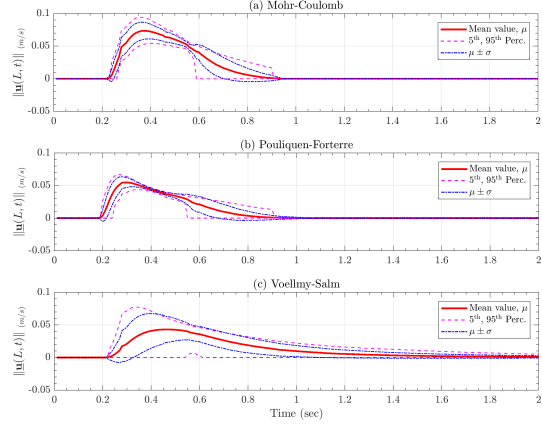
3.1.1 Temporal Records for flowing material (Local Measurements) - Ali



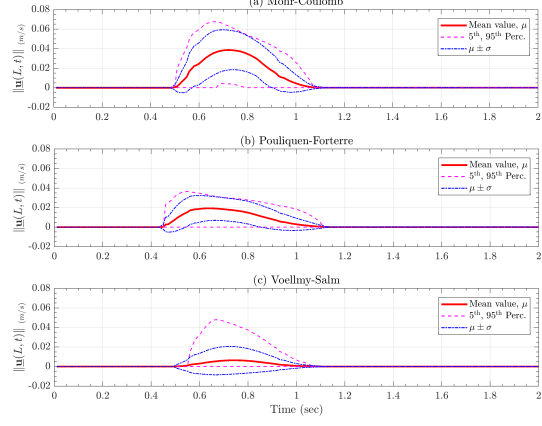
(a) $L = (-0.7, 0)$, .



(c) $L = (0, 0)$, inclined and runout planes' joint location.



(b) $L = (-0.35, 0)$, middle point on inclined plane.



(d) $L = (0.15, 0)$, a location on runout plane.

Figure 2: Records of flow velocity, $\|\mathbf{u}\|(L, t)$.

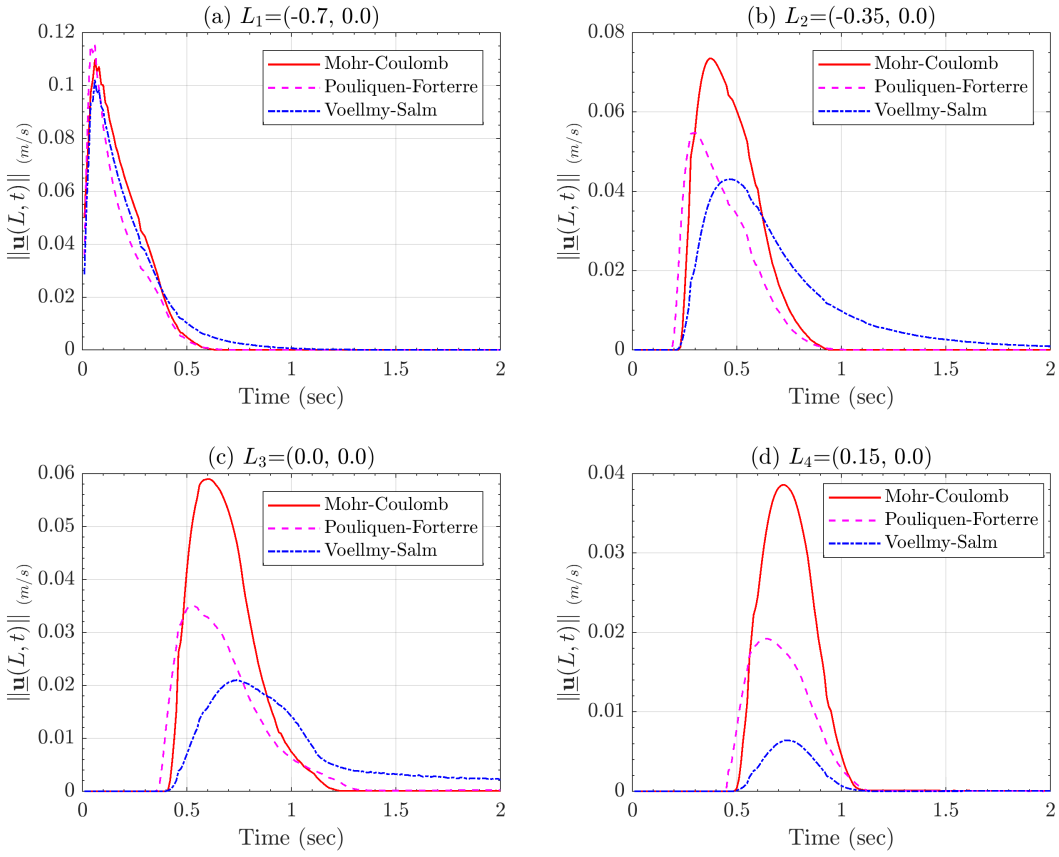
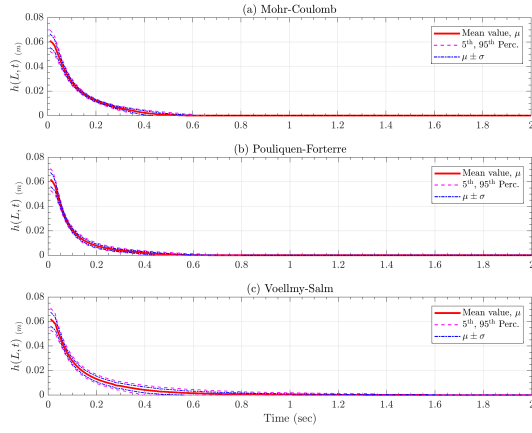
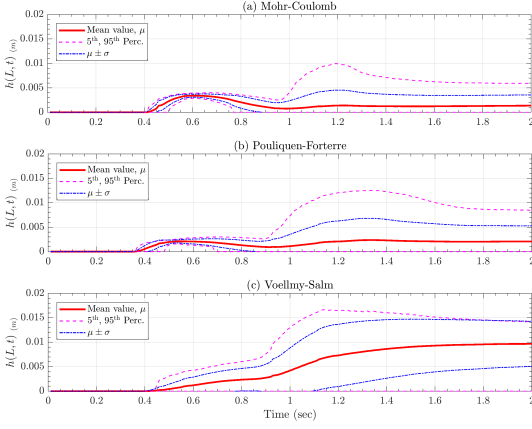


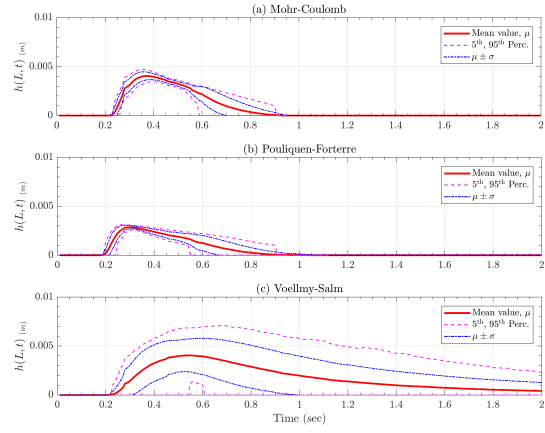
Figure 3: Comparison between mean values of flow velocity, $\|\underline{\mathbf{u}}\|(L, t)$, recorded at locations of interest, L_i , $i=1,\dots,4$.



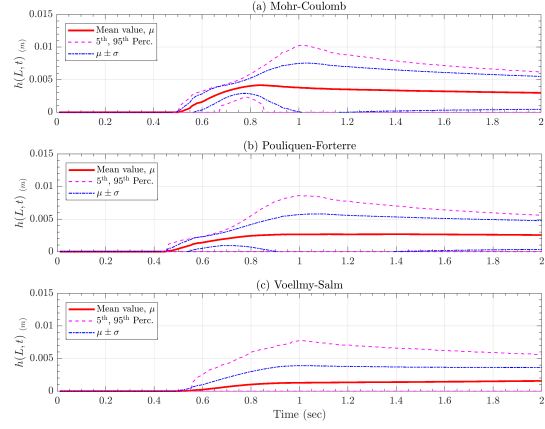
(a) $L = (-0.7, 0)$, slumping pile location.



(c) $L = (0, 0)$, inclined and runout planes' joint location.



(b) $L = (-0.35, 0)$, middle point on inclined plane.



(d) $L = (0.15, 0)$, a location on runout plane.

Figure 4: Records of flow height, $h(L, t)$.

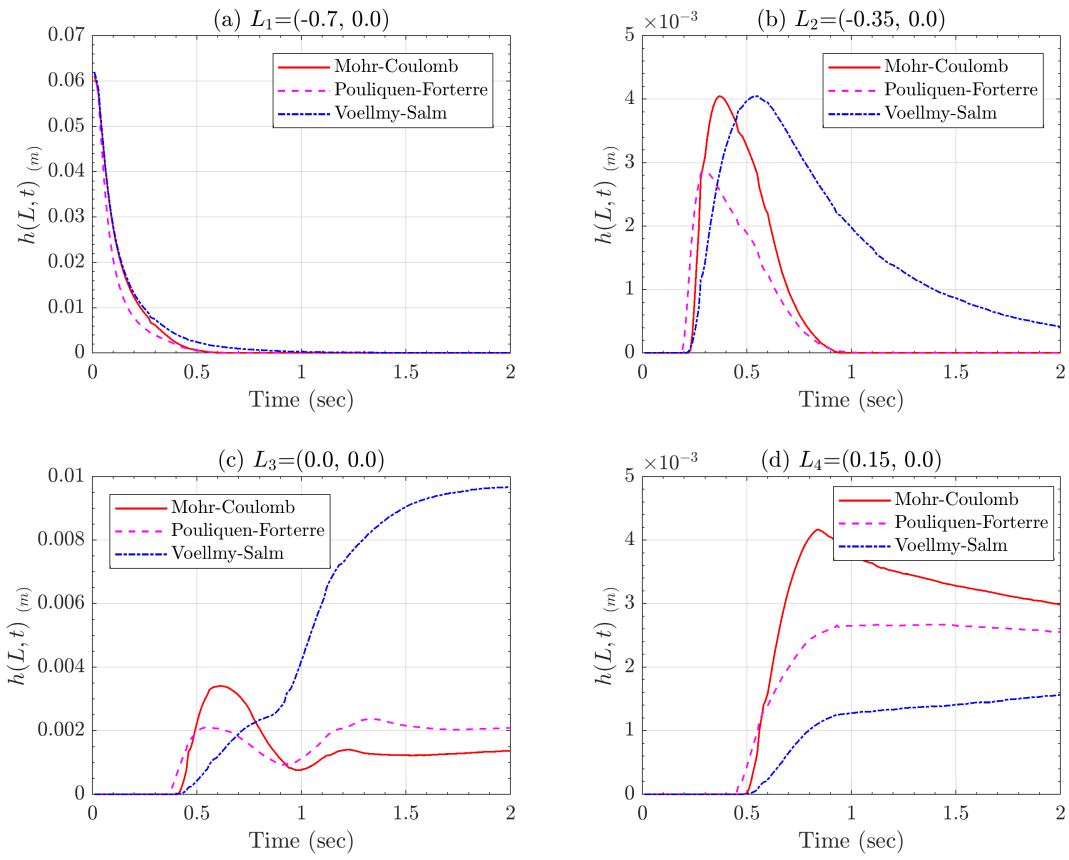
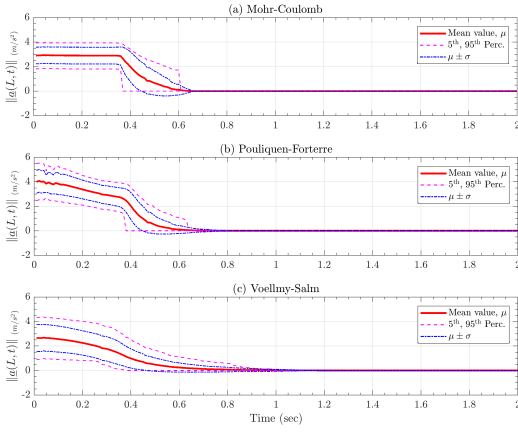
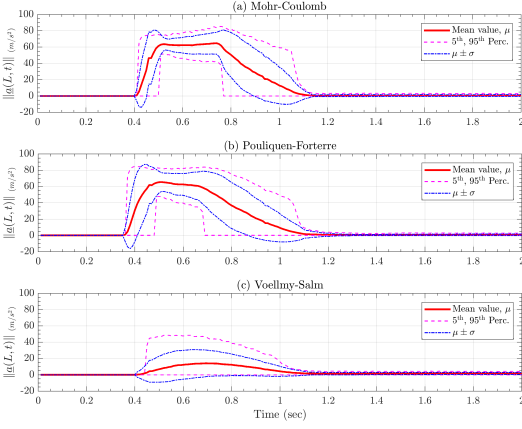


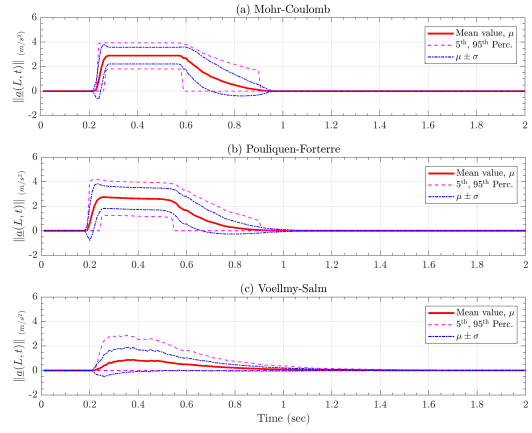
Figure 5: Comparison between mean values of flow height, $h(L, t)$, recorded at locations of interest, L_i , $i=1,\dots,4$.



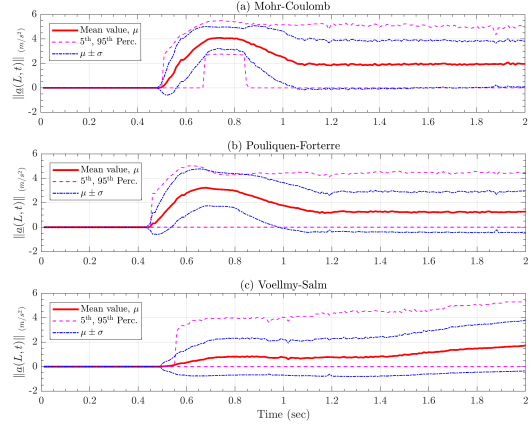
(a) $L = (-0.7, 0)$, slumping pile location.



(c) $L = (0, 0)$, inclined and runout planes' joint location.



(b) $L = (-0.35, 0)$, middle point on inclined plane.



(d) $L = (0.15, 0)$, a location on runout plane.

Figure 6: Records of flow acceleration (computed from RHS), $\|\bar{a}\|(L, t)$.

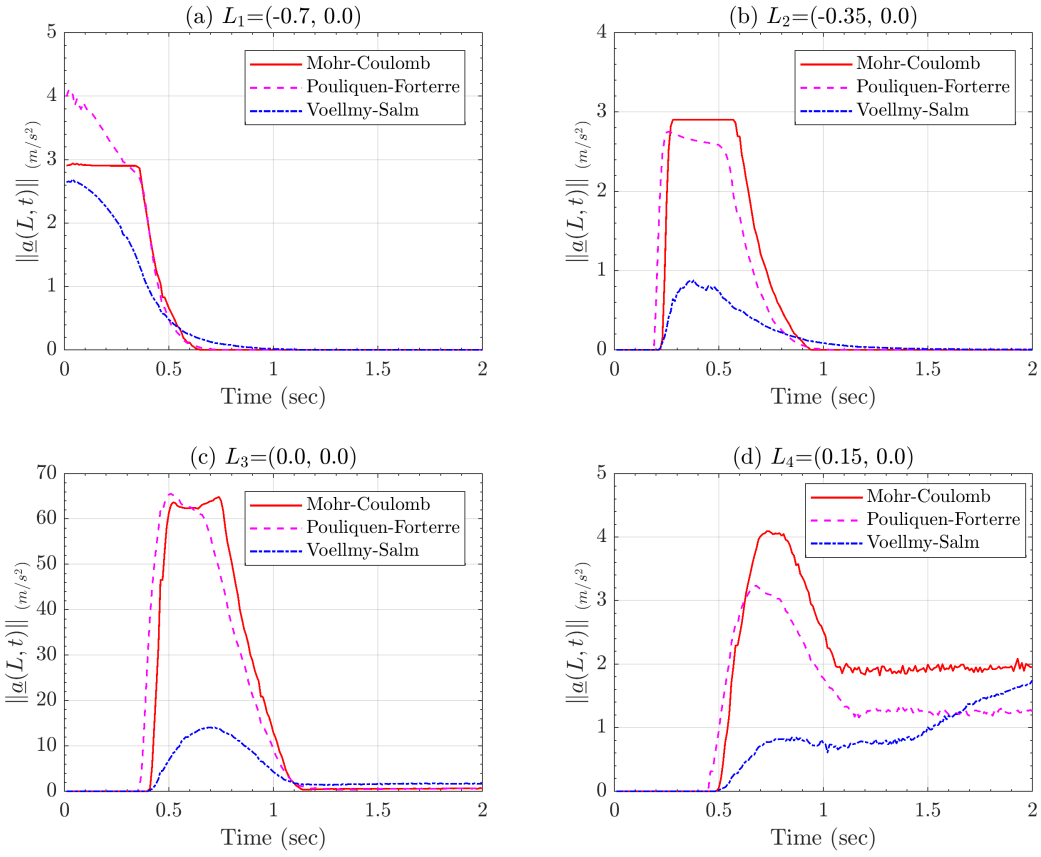
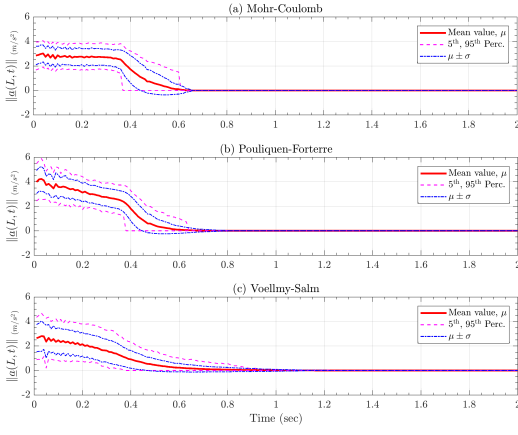
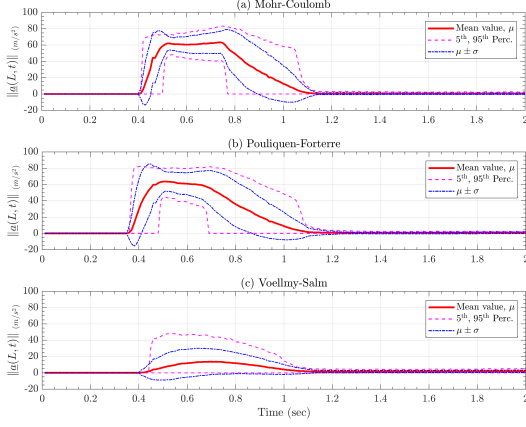


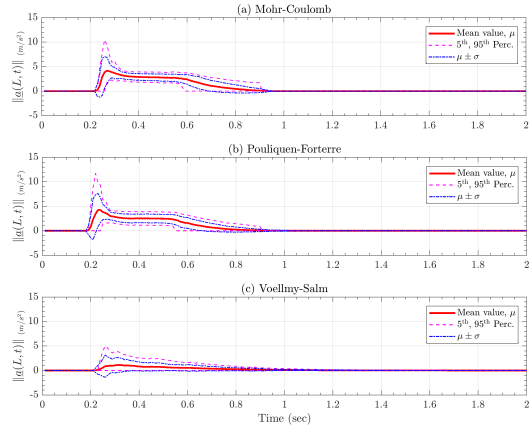
Figure 7: Comparison between mean values of flow acceleration (computed from RHS), $\|\underline{a}\|(L, t)$, recorded at locations of interest, L_i , $i=1,\dots,4$.



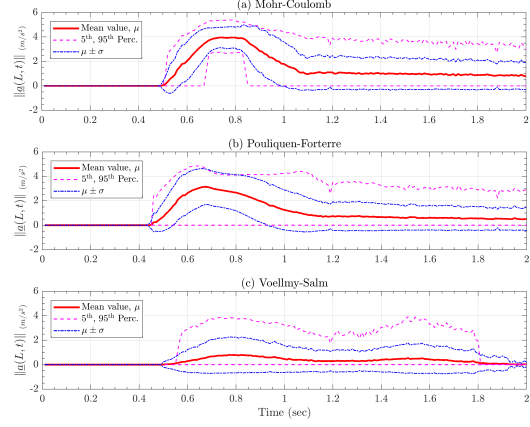
(a) $L = (-0.7, 0)$, slumping pile location.



(c) $L = (0, 0)$, inclined and runout planes' joint location.



(b) $L = (-0.35, 0)$, middle point on inclined plane.



(d) $L = (0.15, 0)$, a location on runout plane.

Figure 8: Records of flow acceleration (computed from LHS), $\|\mathbf{a}\|(L, t)$.

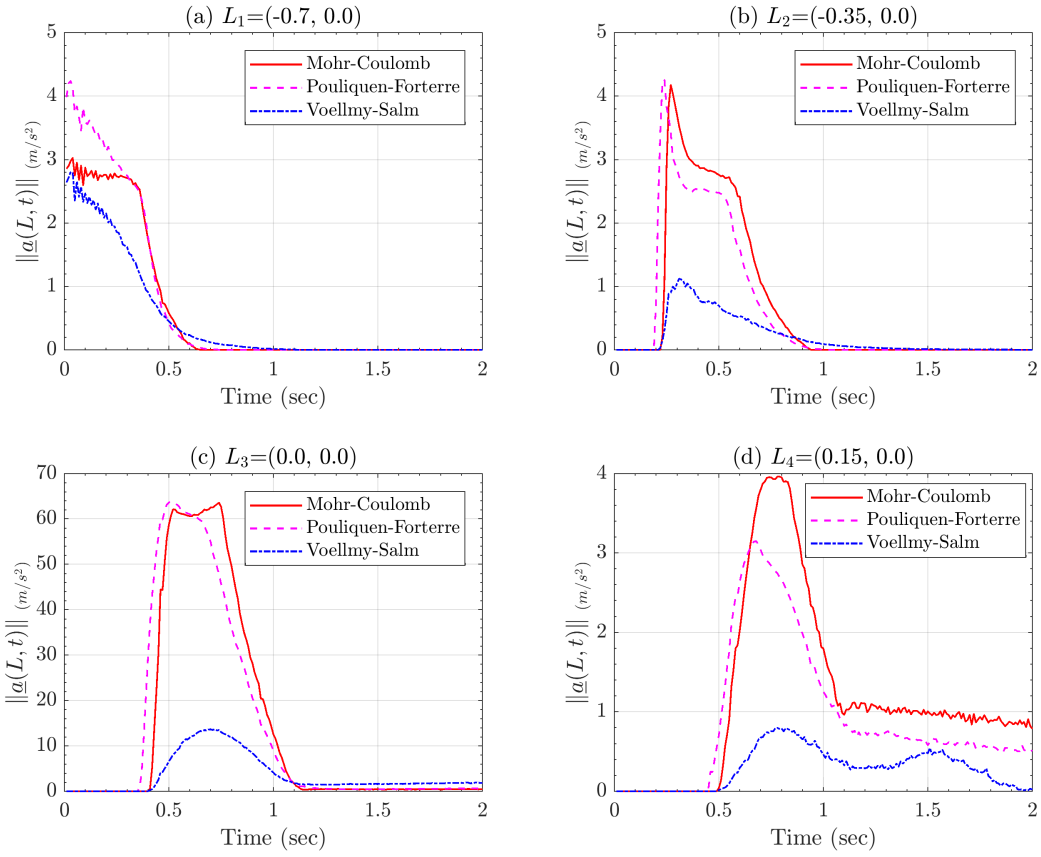


Figure 9: Comparison between mean values of flow acceleration (computed from LHS), $\|\underline{a}\|(L, t)$, recorded at locations of interest, L_i , $i=1, \dots, 4$.

3.1.2 Temporal Records for Bulk of flowing material (Spatial averages) - Ali

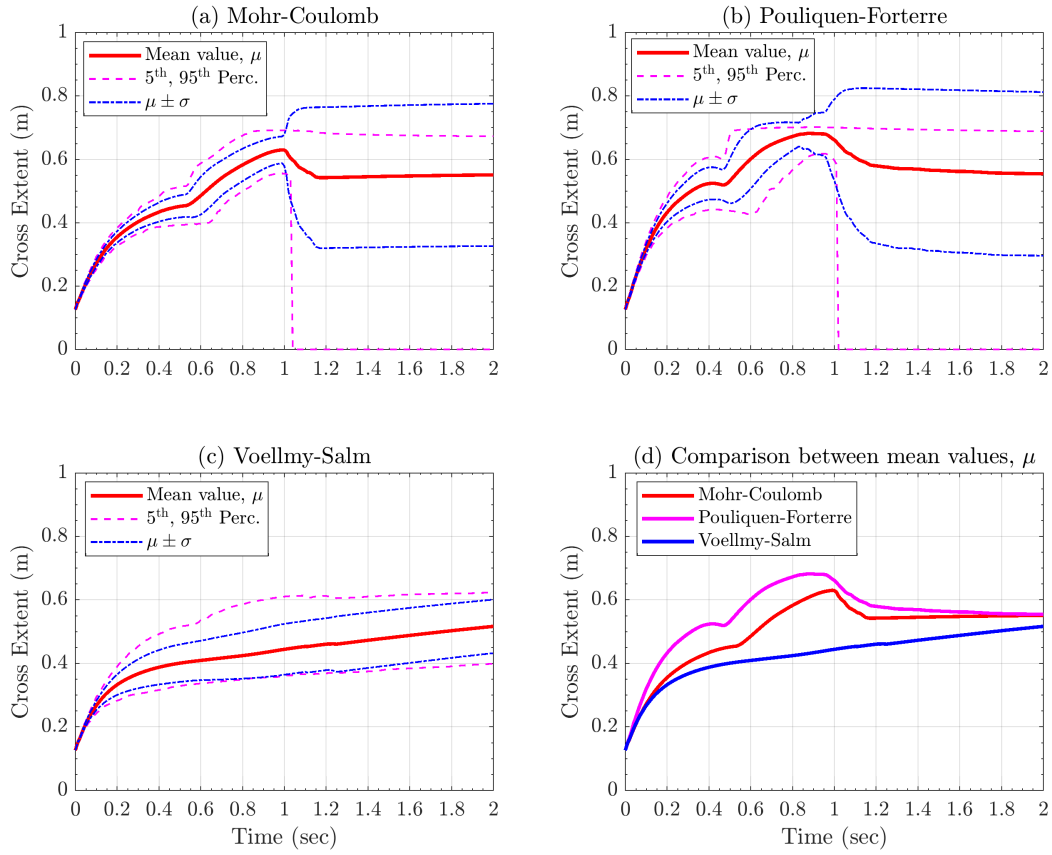


Figure 10: Full statistics for temporal records of maximum flow extent along the lateral directions.

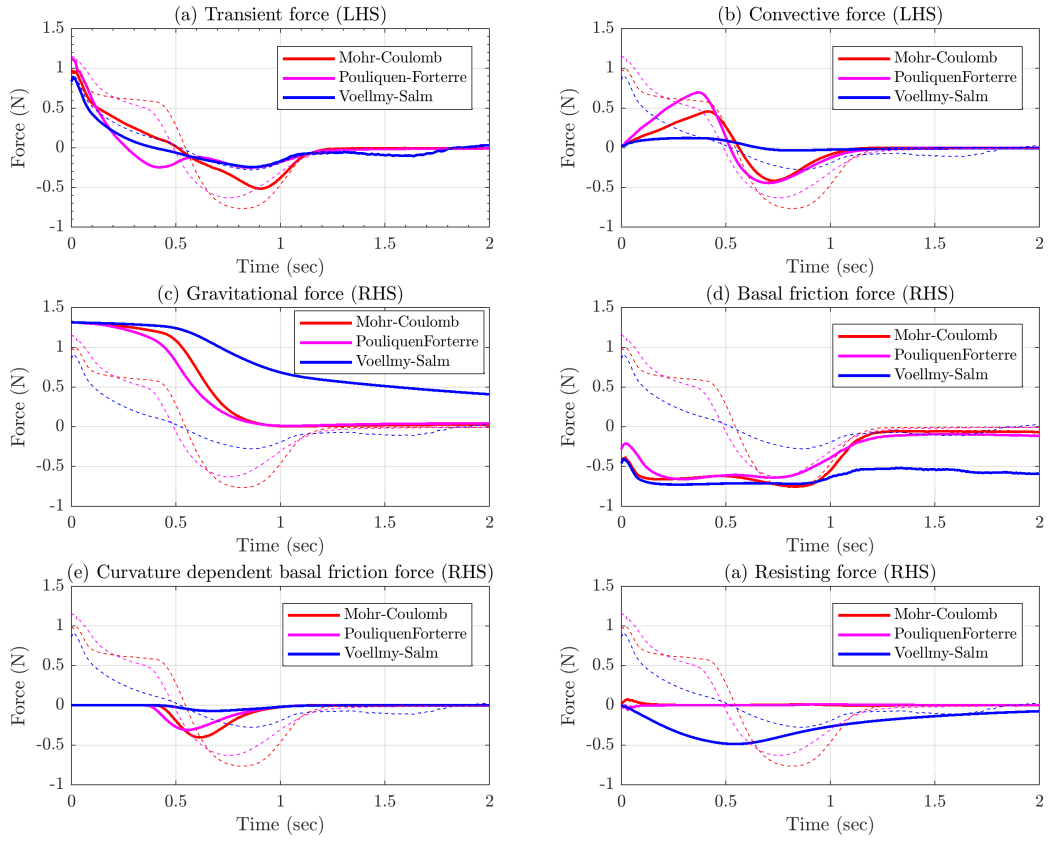


Figure 11: Full statistics for temporal records of mean values of all sources of force along the runout direction. Dashed lines are the total forces related to each model.

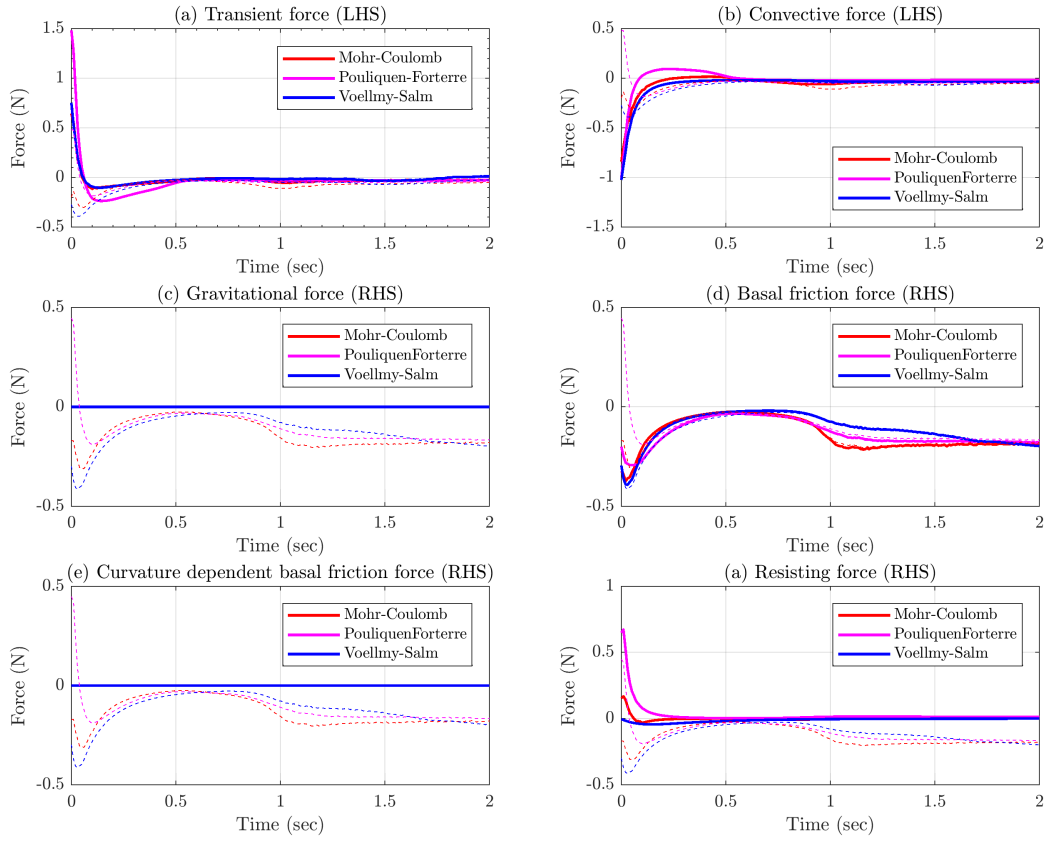


Figure 12: Full statistics for temporal records of mean values of all sources of force along the lateral direction. Dashed lines are the total forces related to each model.

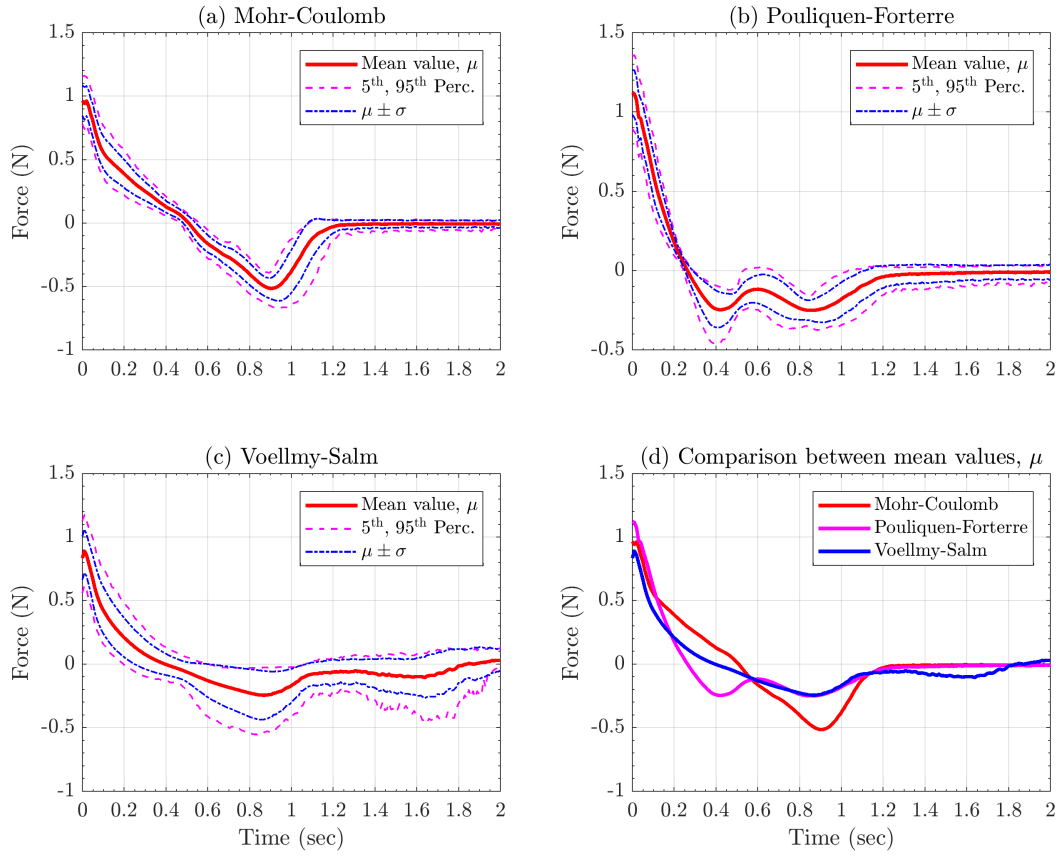


Figure 13: Full statistics for temporal records of transient force (LHS) along the runout direction.

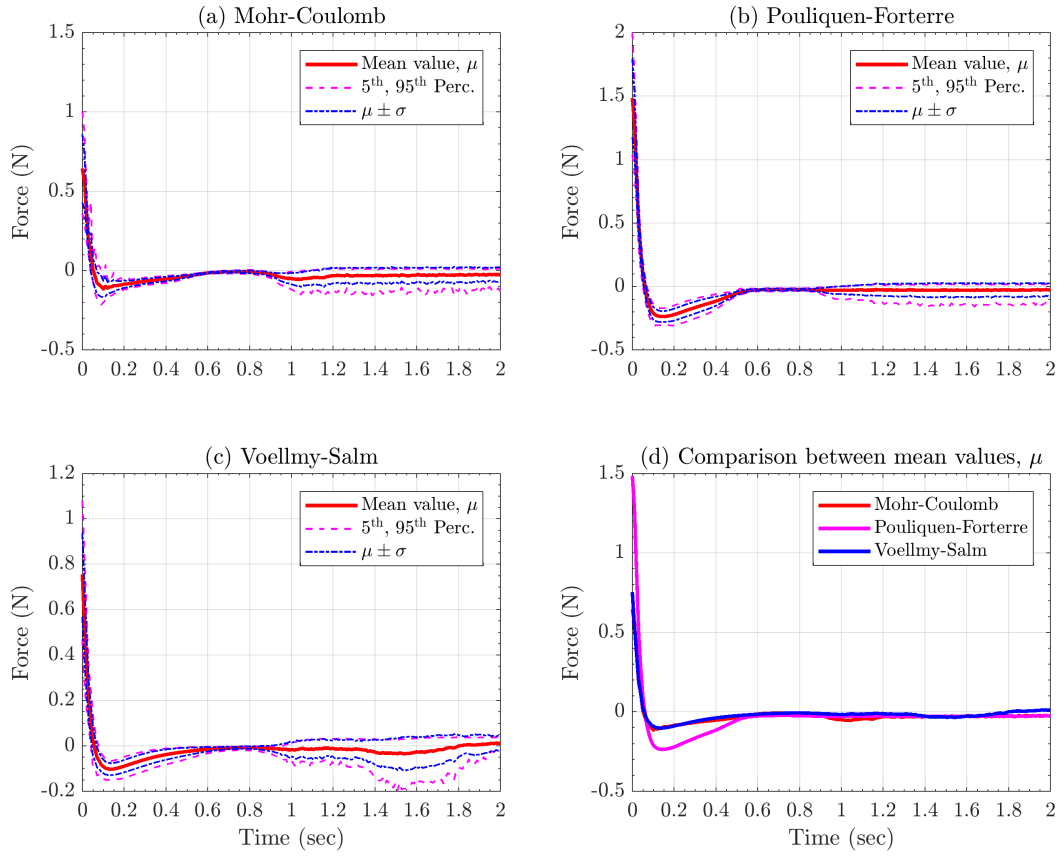


Figure 14: Full statistics for temporal records of transient force (LHS) along the lateral direction.

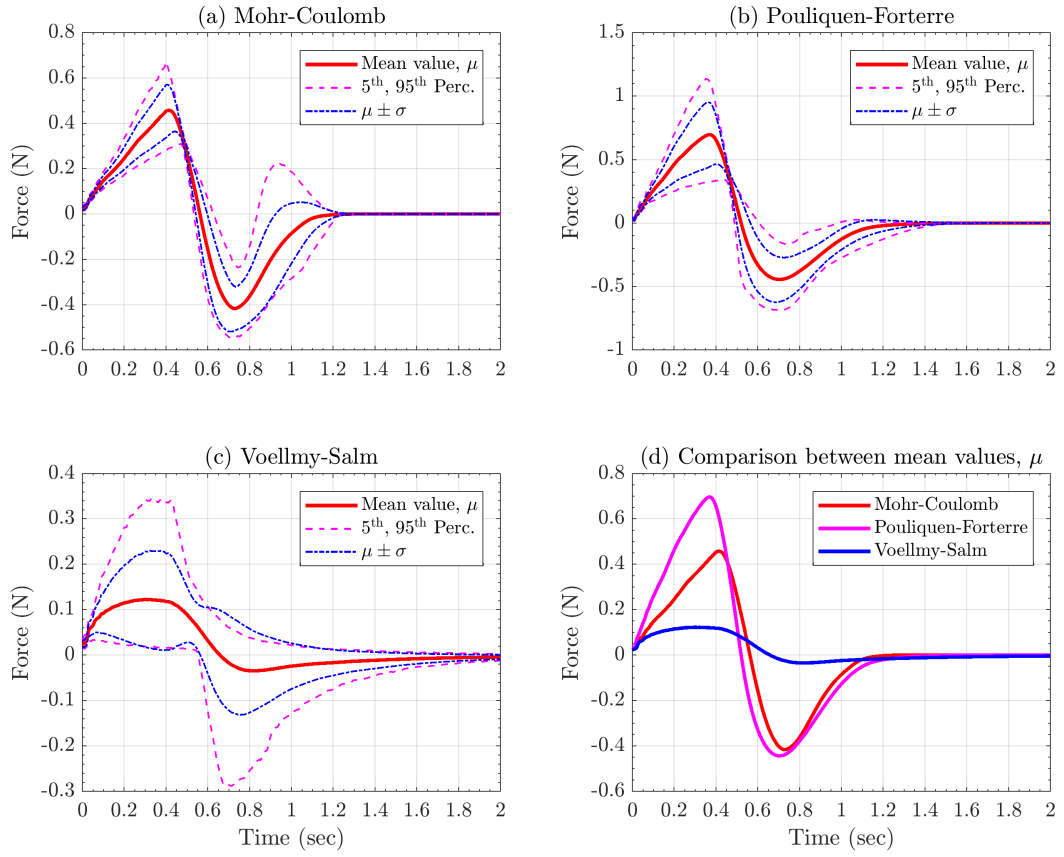


Figure 15: Full statistics for temporal records of convective force (LHS) along the runout direction.

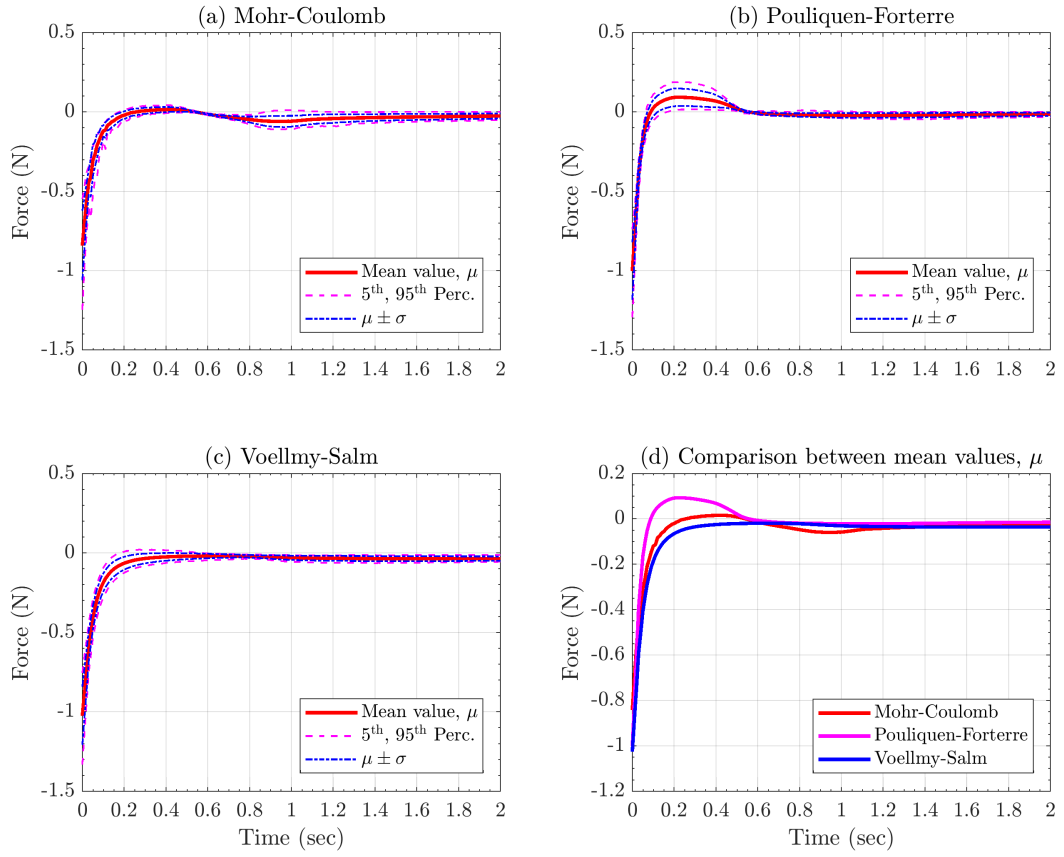


Figure 16: Full statistics for temporal records of convective force (LHS) along the lateral direction.

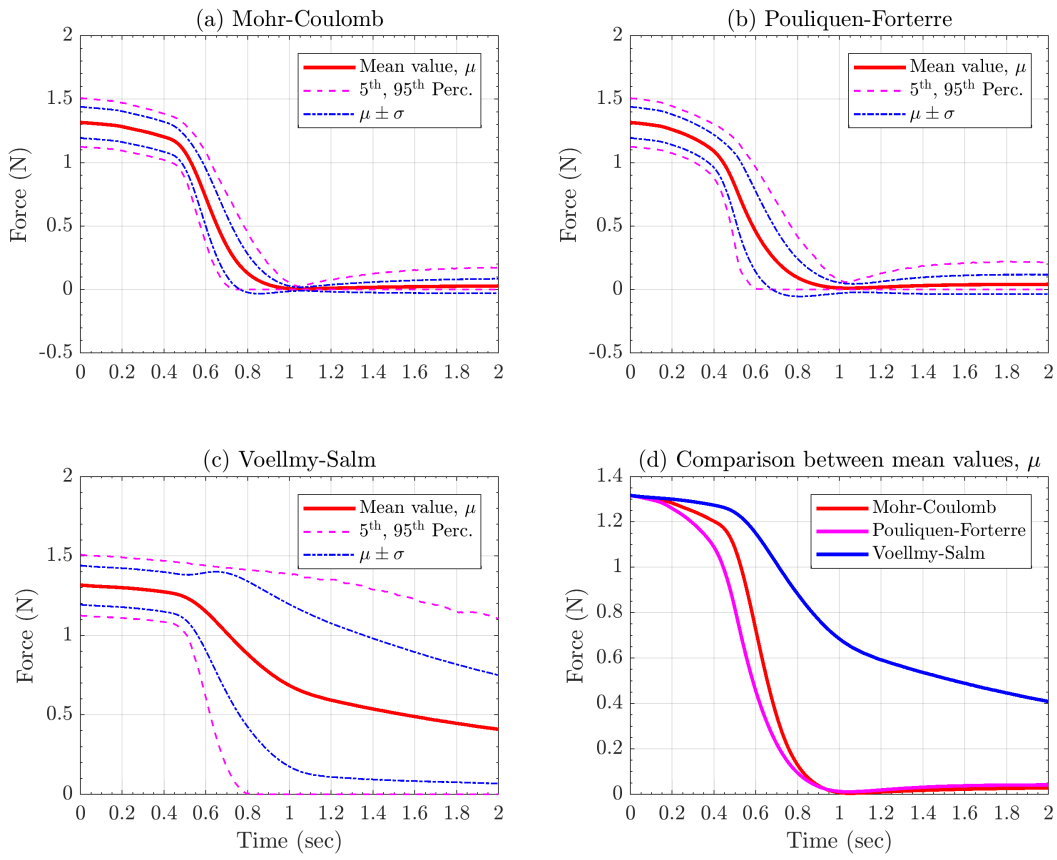


Figure 17: Full statistics for temporal records of gravitational force (RHS) along the runout direction.

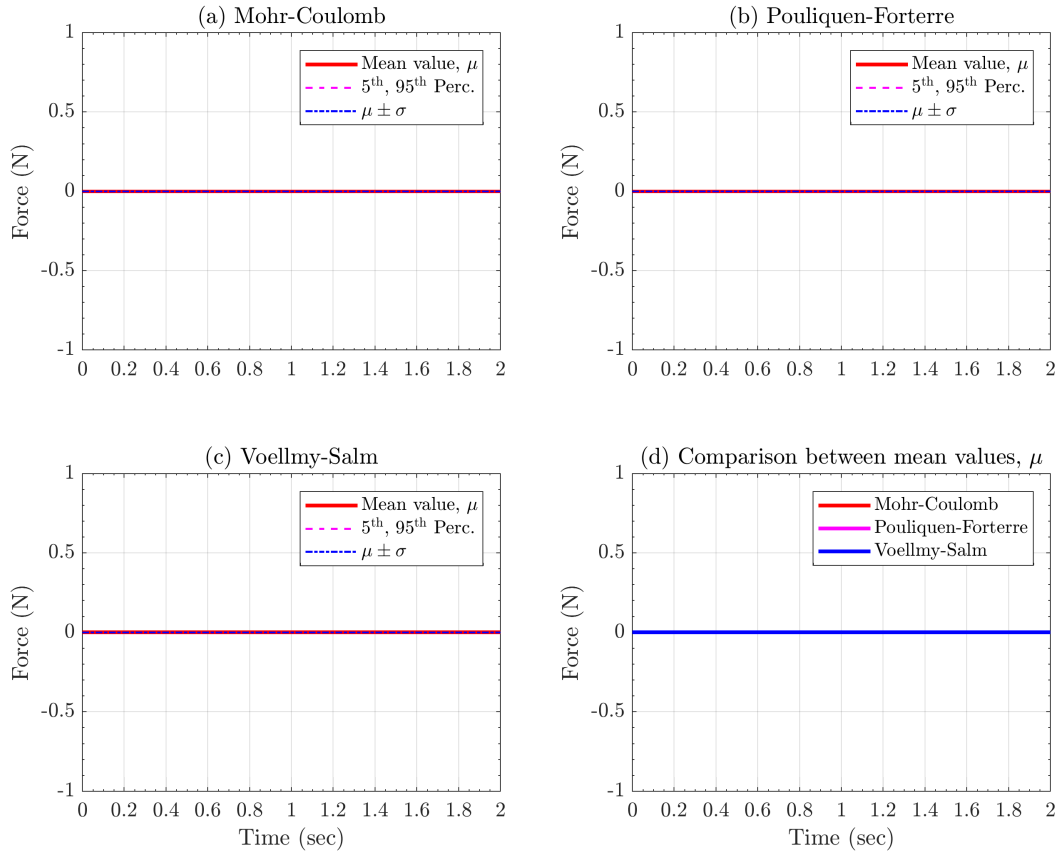


Figure 18: Full statistics for temporal records of gravitational force (RHS) along the lateral direction.

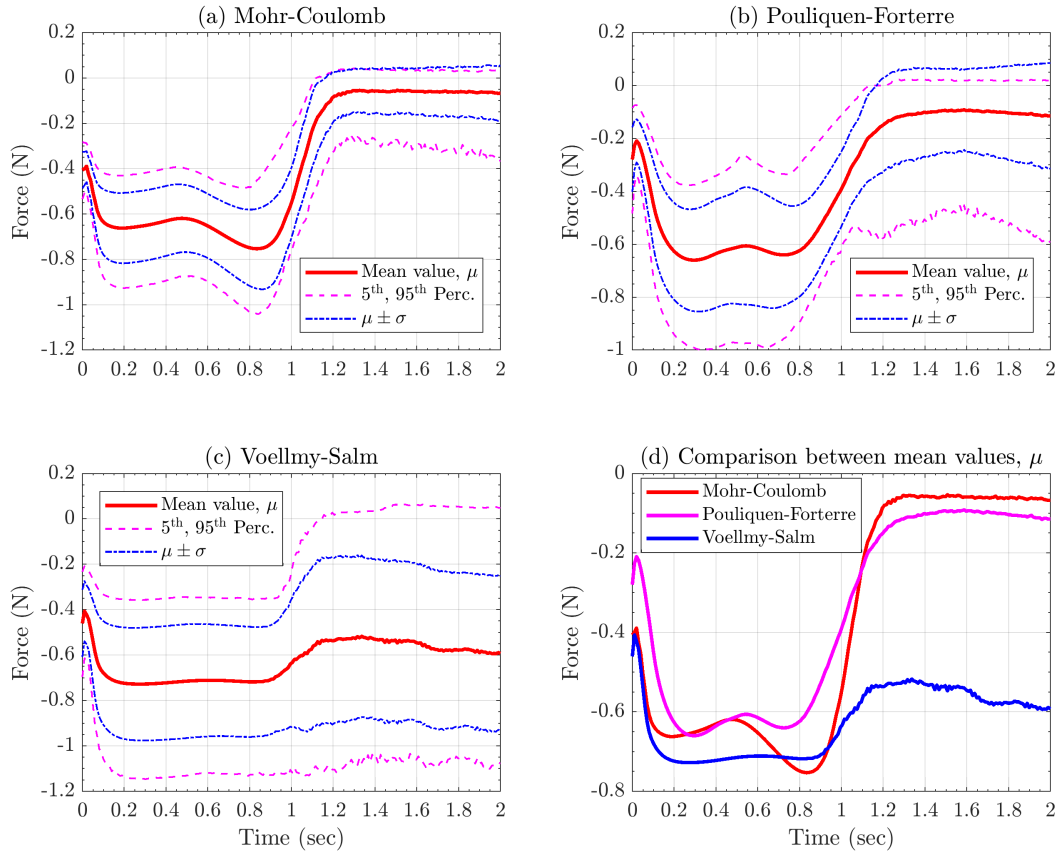


Figure 19: Full statistics for temporal records of bed friction force (RHS) along the runout direction.

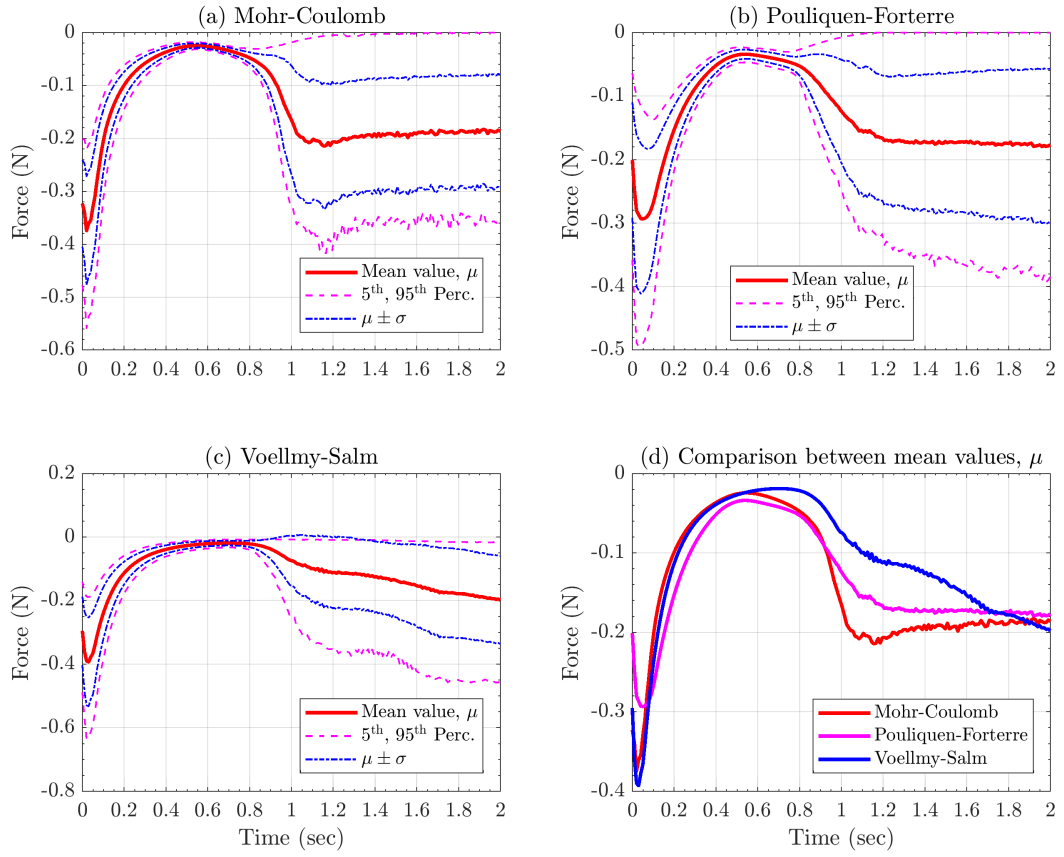


Figure 20: Full statistics for temporal records of bed friction force (RHS) along the lateral direction.

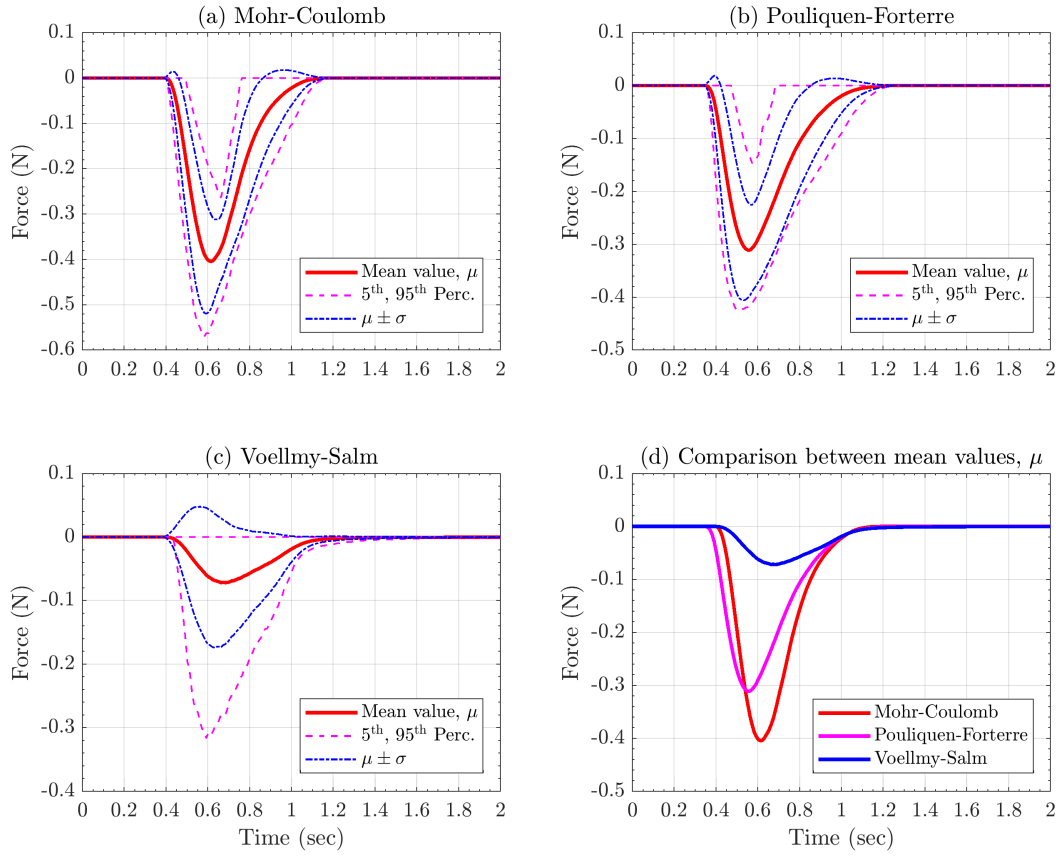


Figure 21: Full statistics for temporal records of curvature based bed friction force (RHS) along the runout direction.

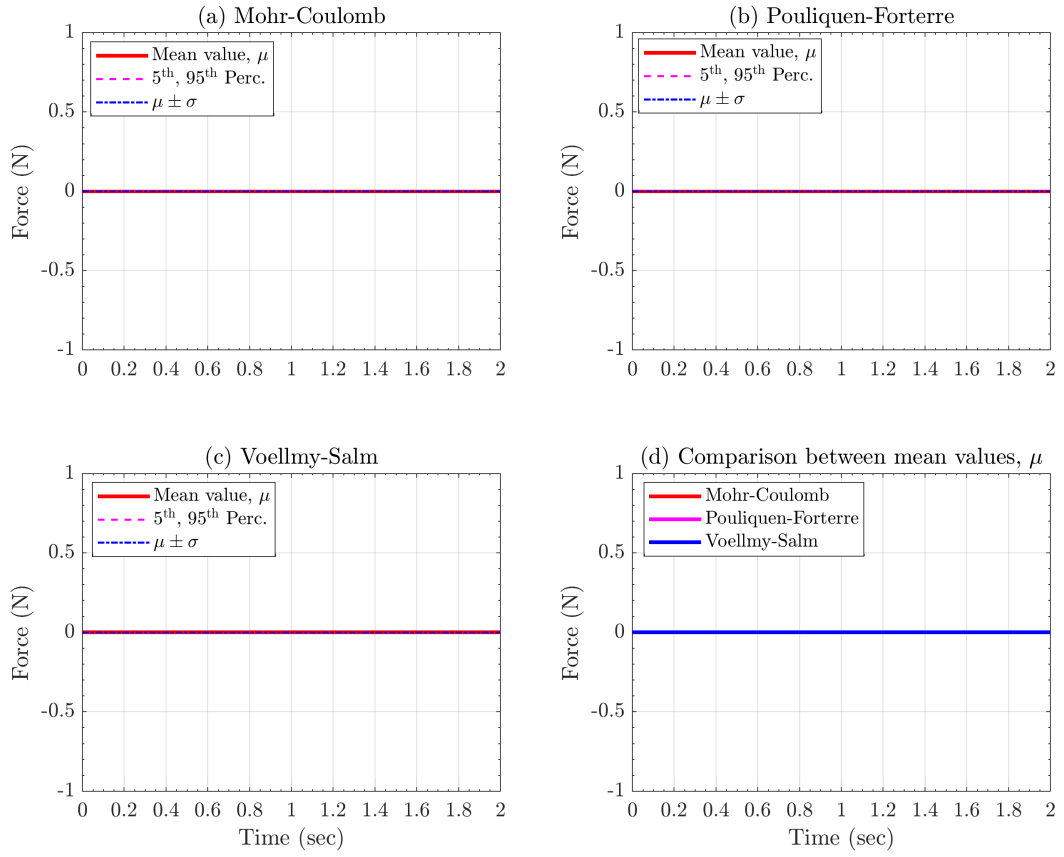


Figure 22: Full statistics for temporal records of curvature based bed friction force (RHS) along the lateral direction.

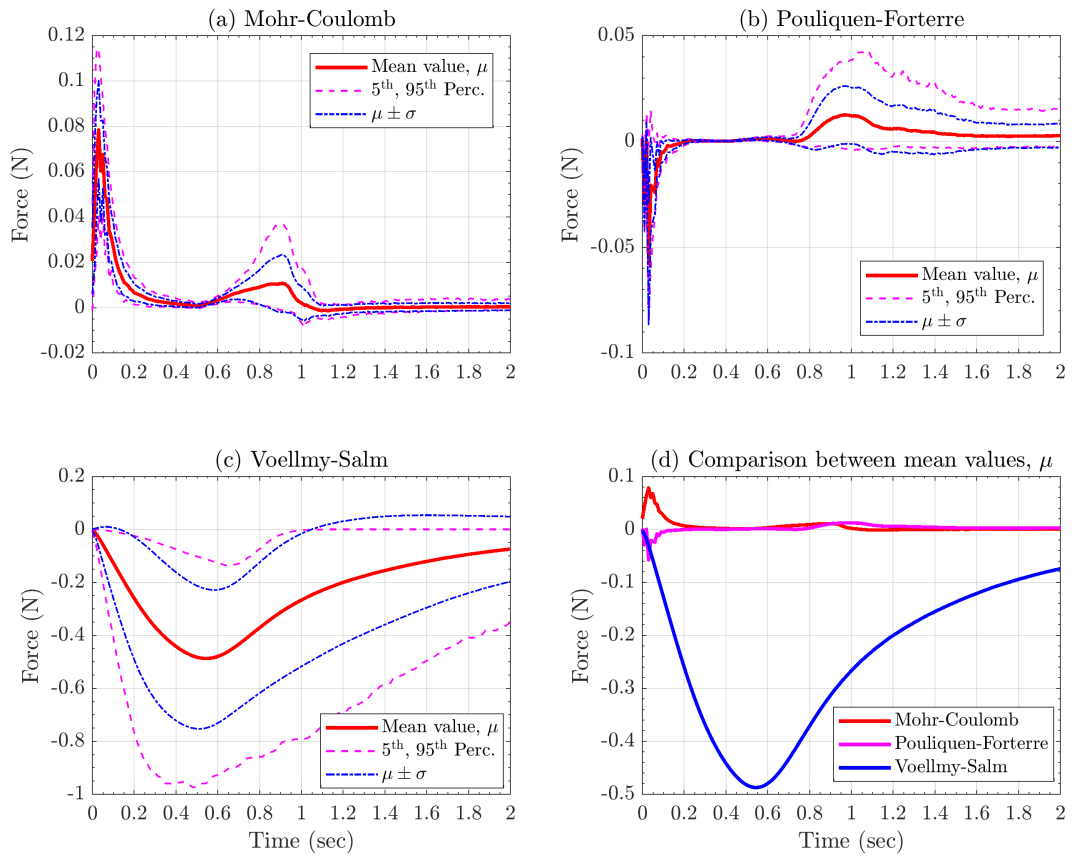


Figure 23: Full statistics for temporal records of other resisting force (RHS) along the runout direction.

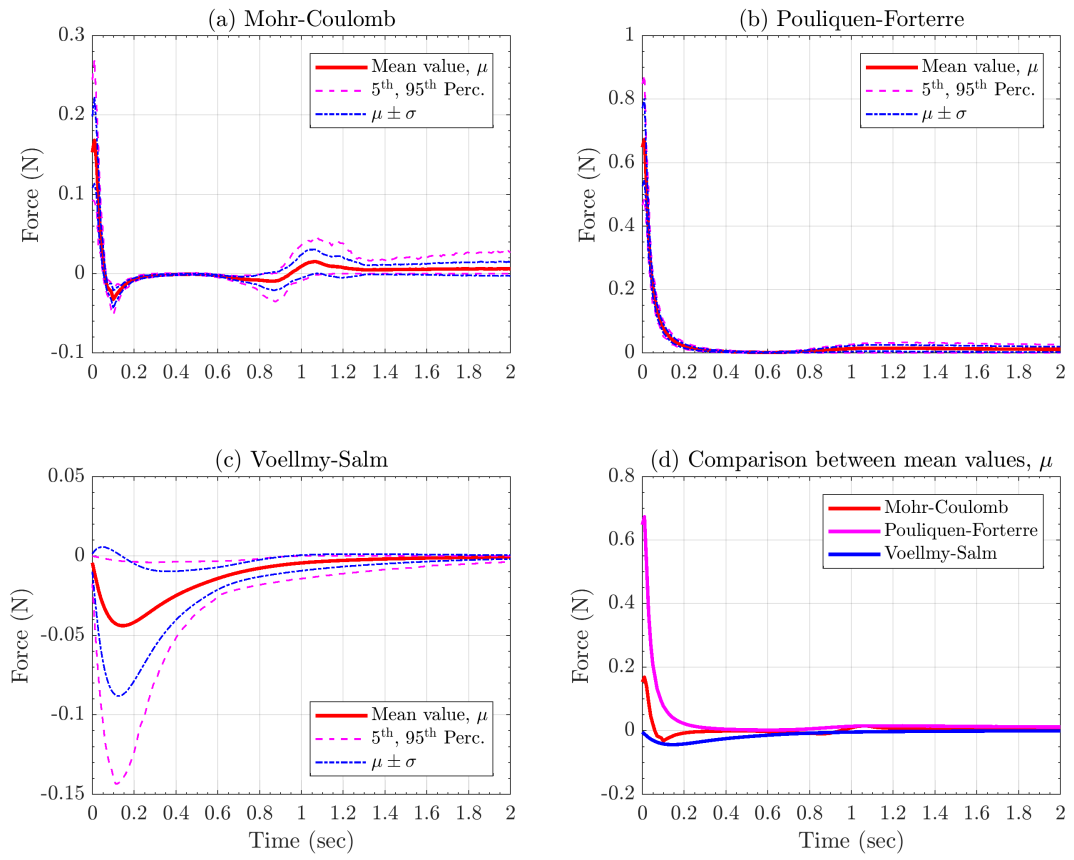


Figure 24: Full statistics for temporal records of other resisting force (RHS) along the lateral direction.

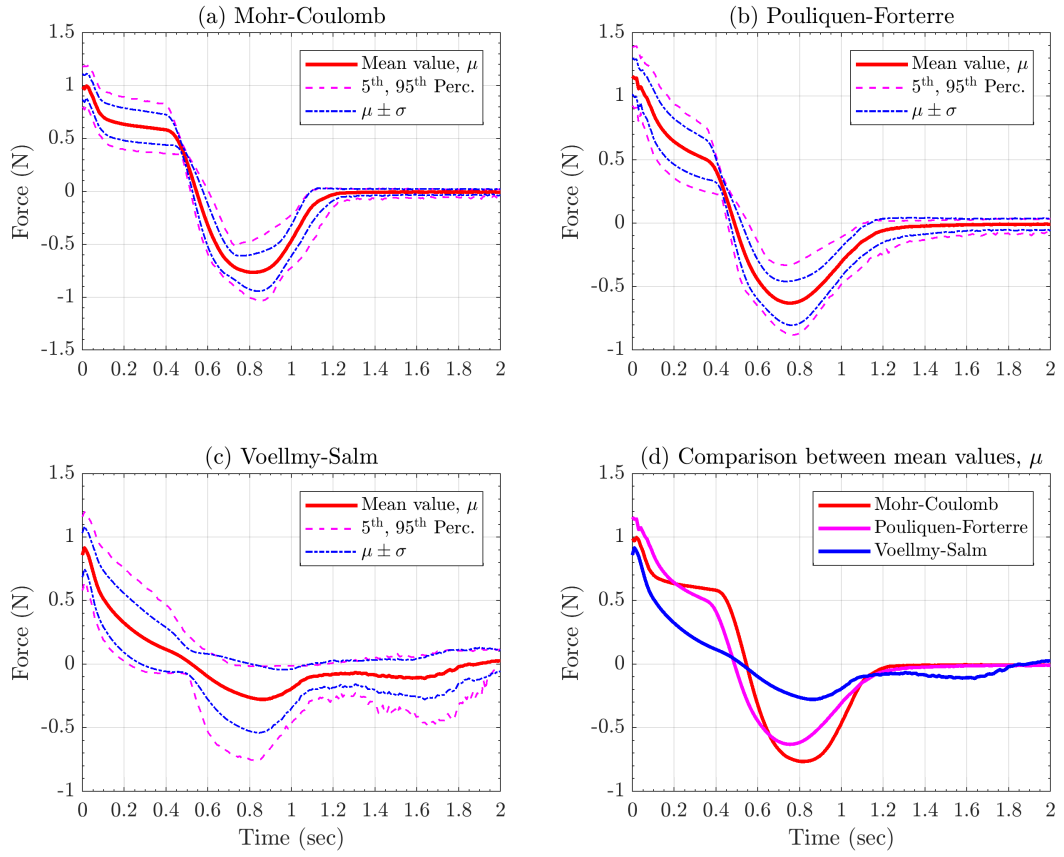


Figure 25: Full statistics for temporal records of the total force (RHS) along the runout direction.

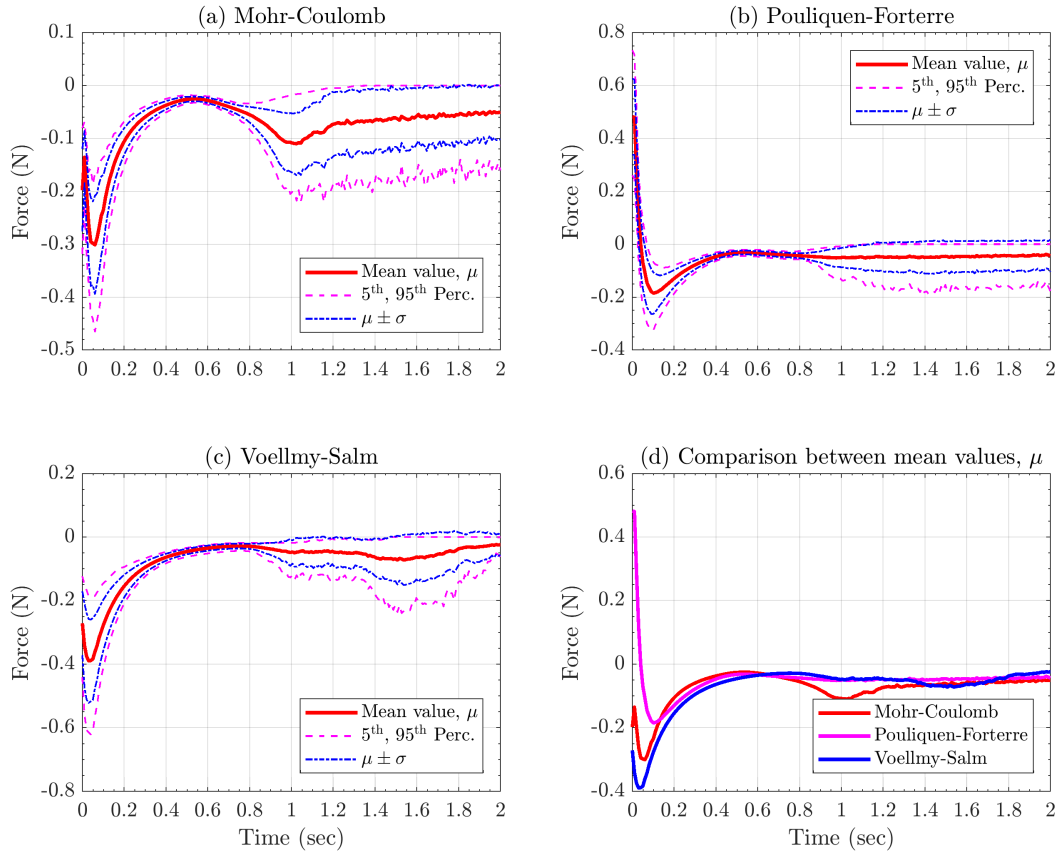


Figure 26: Full statistics for temporal records of the total force (RHS) along the lateral direction.

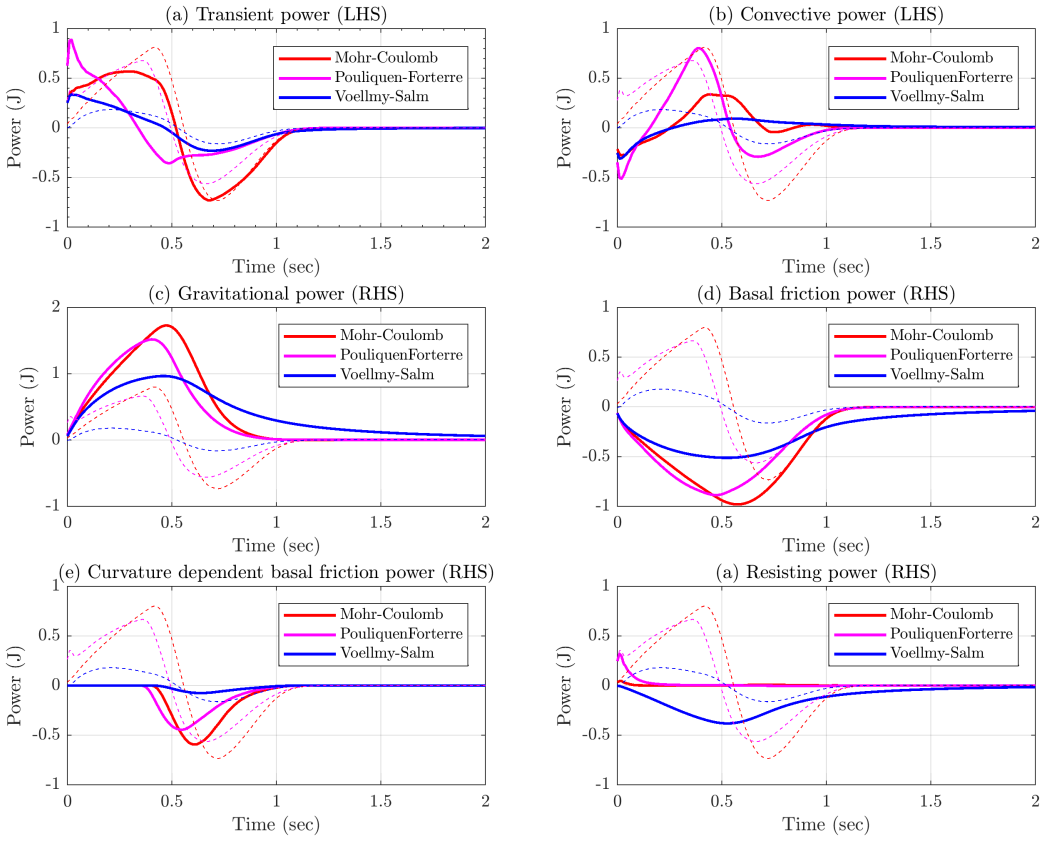


Figure 27: Full statistics for temporal records of mean values of all sources of power. Dashed lines are the total powers related to each model.

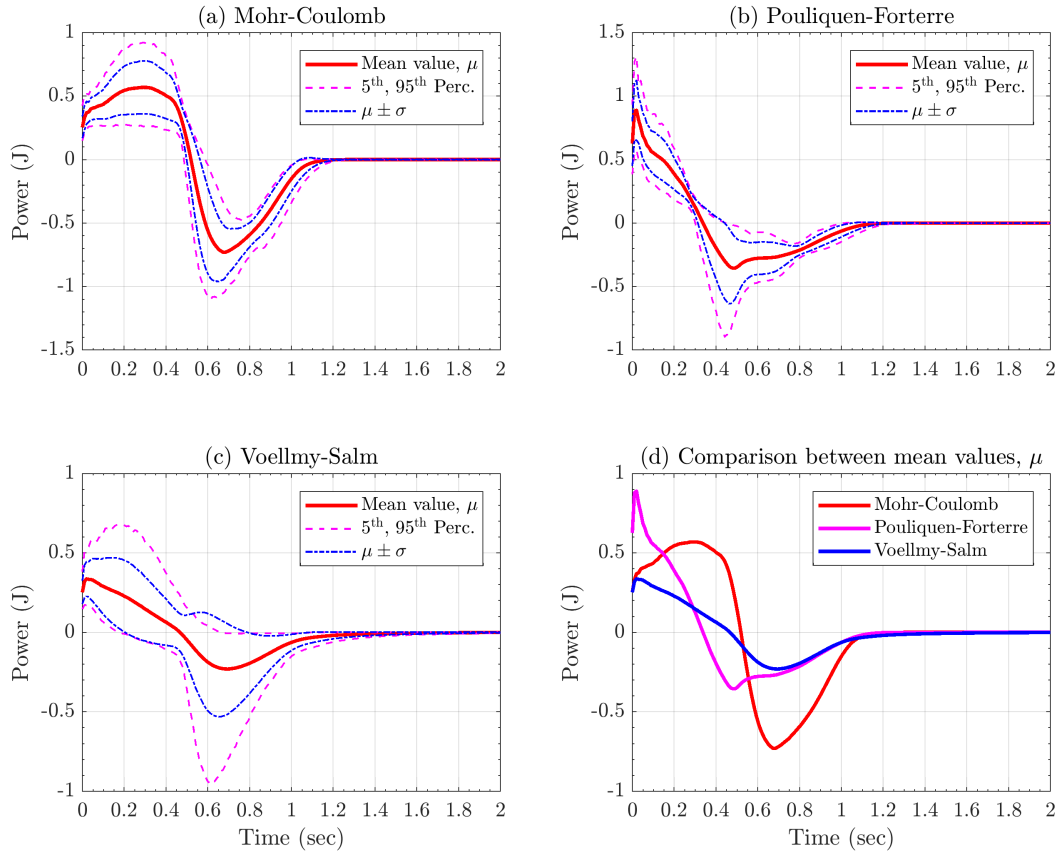


Figure 28: Full statistics for temporal records of power by transient forces.

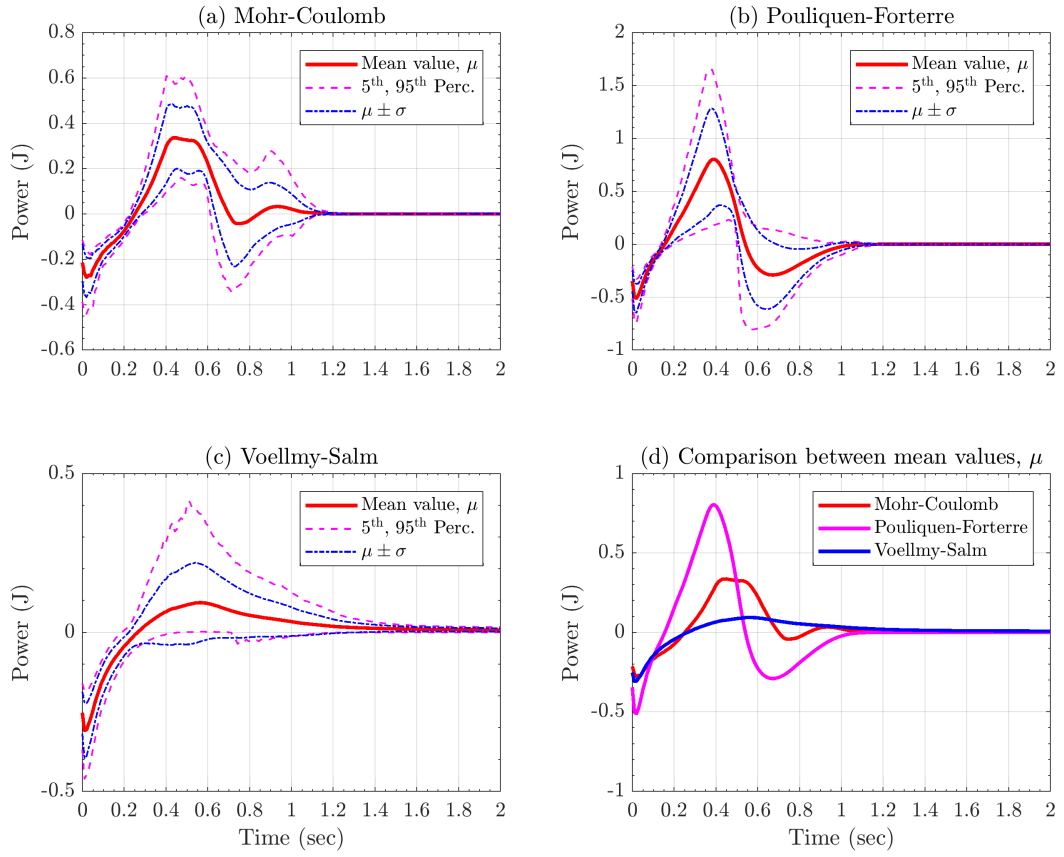


Figure 29: Full statistics for temporal records of power by convective forces.

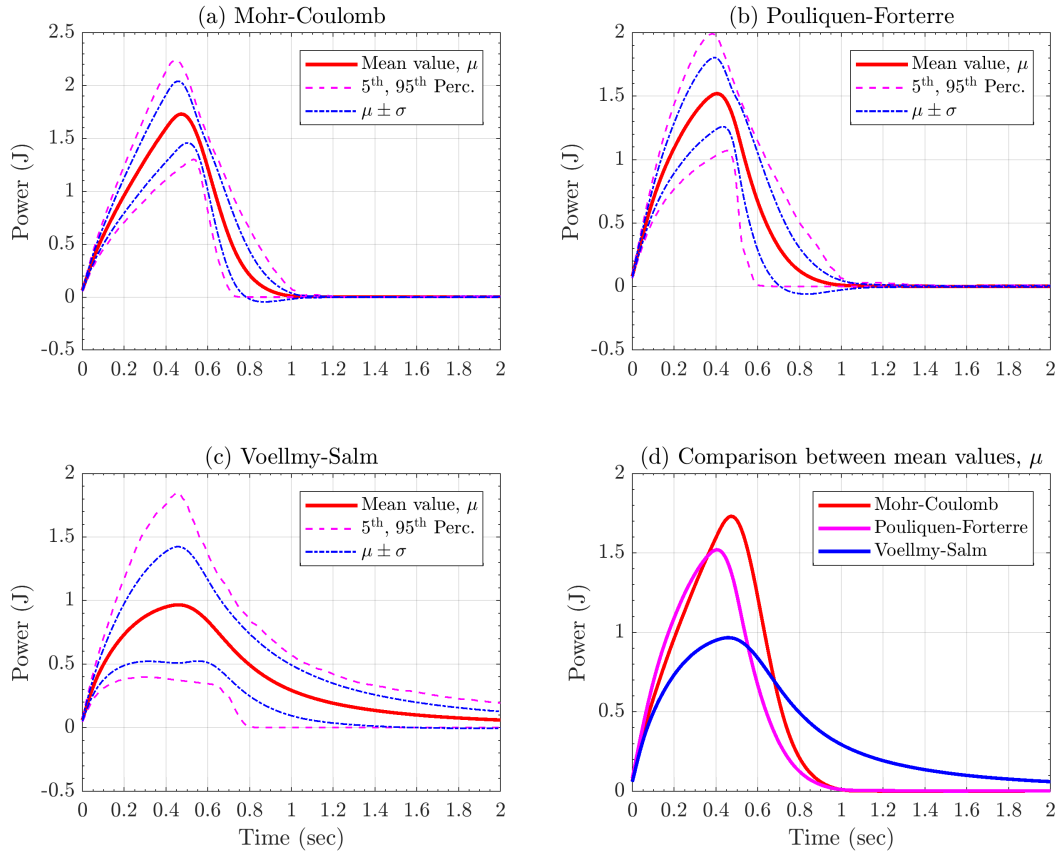


Figure 30: Full statistics for temporal records of power by gravitational forces.

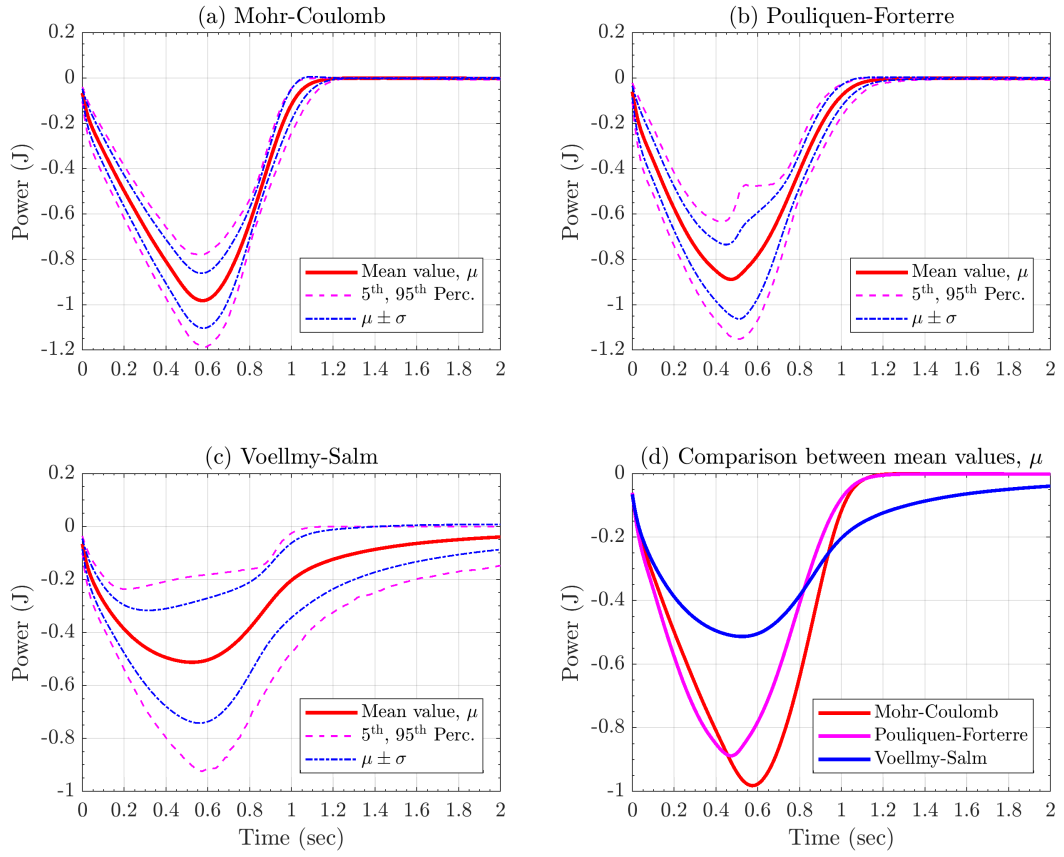


Figure 31: Full statistics for temporal records of power by bed friction forces.

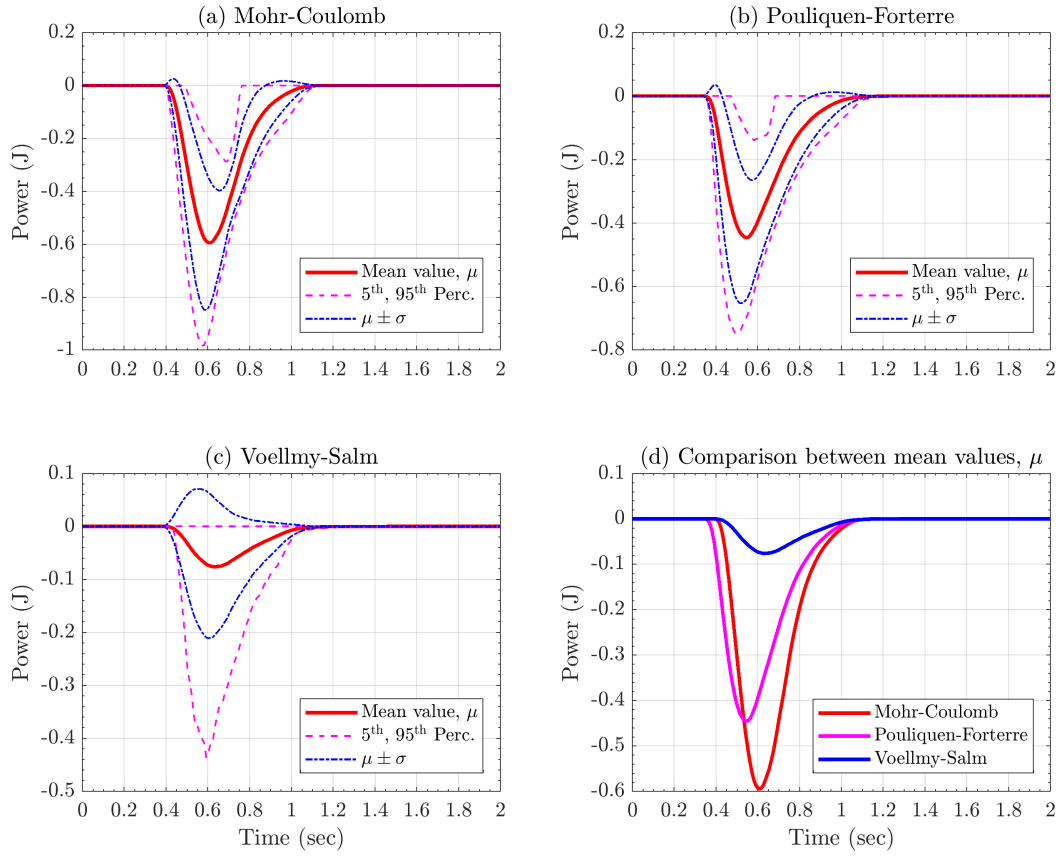


Figure 32: Full statistics for temporal records of power by curvature based bed friction forces.

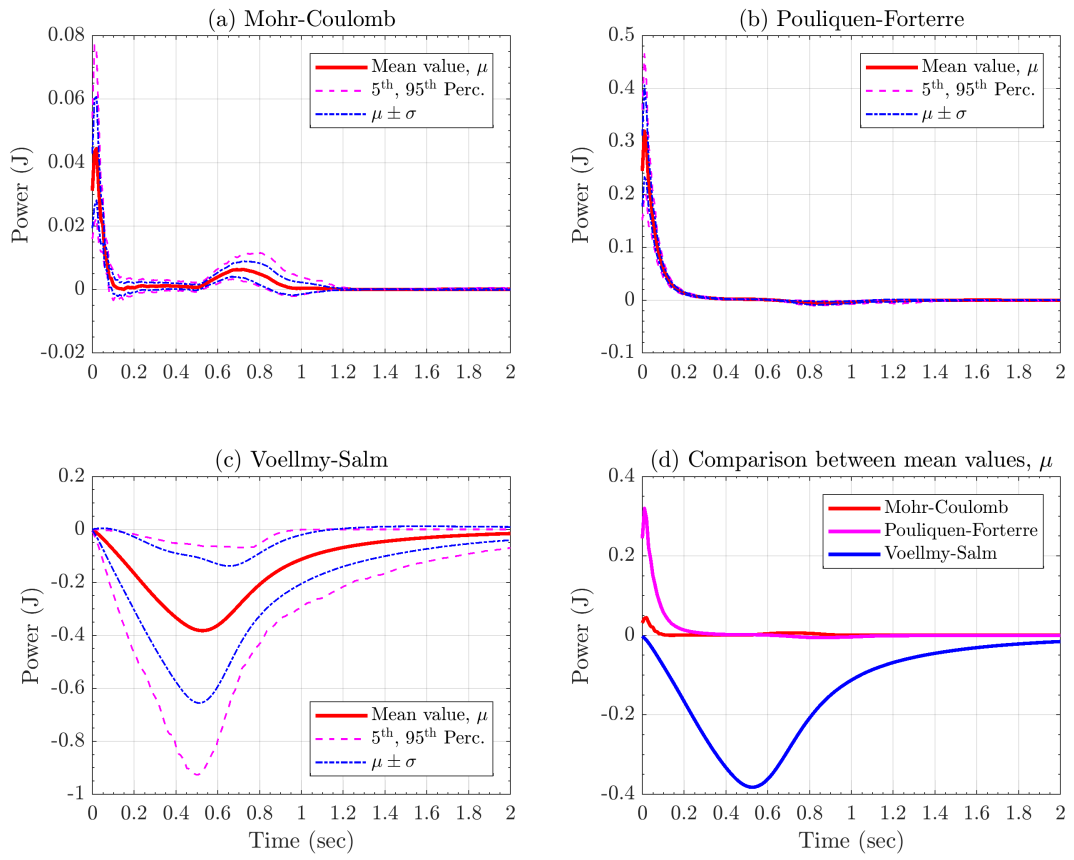


Figure 33: Full statistics for temporal records of power by other source of resisting forces.

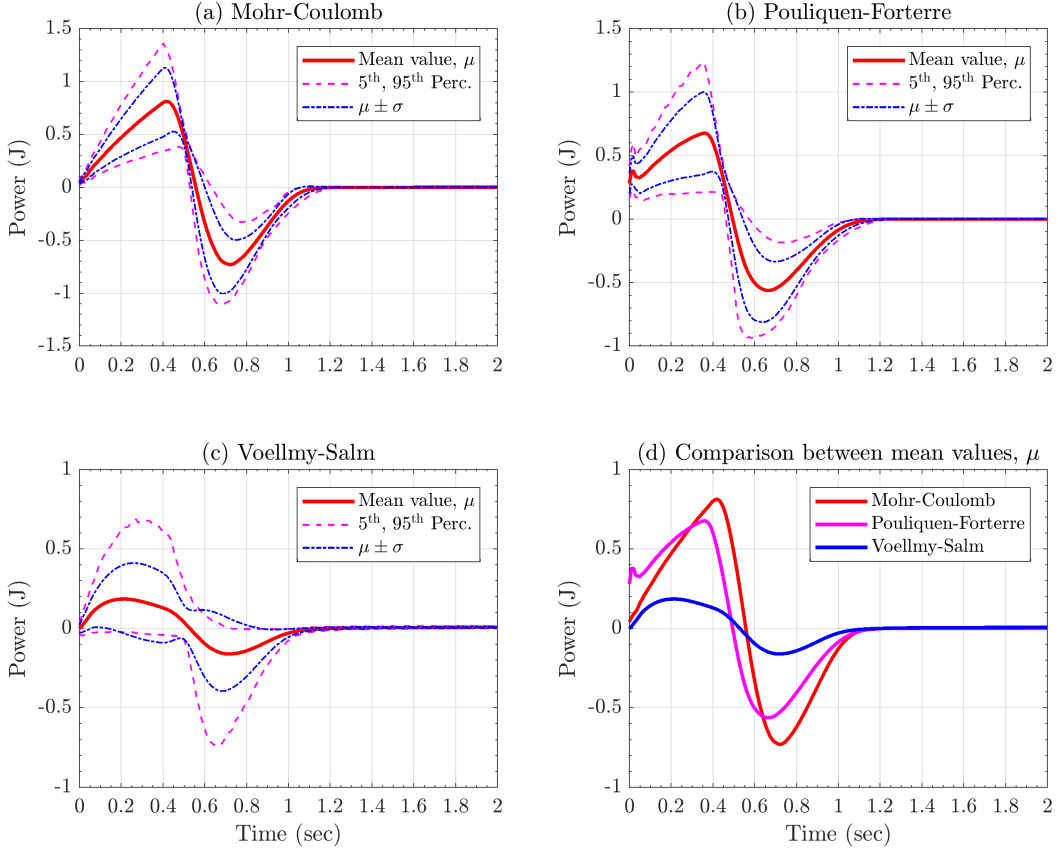


Figure 34: Full statistics for temporal records of power by total external forces (RHS).

3.1.3 Force contributions - Andrea+Ali

A statistical analysis capable of measuring the contributions of different force components in the rheology models is a fundamental task. This is also necessary to explore and compare the effects of the assumptions behind some modeling choices, onto the time evolution of the flowing material. Let $(F_i(x, t))_{i=1, \dots, n}$ be the array of force components, where $x \in \mathbb{R}^2$ is a spatial location, and $t \in T$ is a time instant. In our case study, F_1 is the gravitational force, F_2 is the basal friction, F_3 is the curvature correction, F_4 is a resistant force (or the hydrostatic pressure term, in the case of Pouliquen-Forterre rheology). However, this type of procedure can be applied to any additive decomposition of the physical forces. In addition, we can include in the analysis also the component of the inertial forces, i.e. F_4 the convective force and F_5 the transient force. The analysis of local effects can be compared to the contribution of global dynamics.

In this case we are projecting the forces on the directions X and Y, i.e. respectively in the slope direction, and orthogonal to the slope direction on an horizontal plane. Hence in the following the forces are scalar and not vectorial terms. It is important to remark that all the forces are depending on the sample η on the parameter domains, and hence are considered as random variables.

The degree of contribution of those force terms is significantly variable in space and time. For this reason, the following analysis is performed on locally sampled measurements, and not in a spatial averaging framework. In particular, four locations are selected among the center line of the flow. These are: the initial pile location $x_1 = -0.7$ m, the middle of the inclined plane $x_2 = -0.35$ m, the change in slope $x_3 = 0$ m, the middle of the flat plane $x_4 = 0.15$ m. Next notation will assume to be in a selected location $x = x_k$, where $k \in \{1, \dots, 4\}$. The definitions are not depending on the location, but all the

results will significantly depend of that choice.

Definition 1 (Contribution coefficients) Let $(F_i)_{i=1,\dots,n}$ be random variables on (Ω, \mathcal{F}, P) , representing the considered force components in location x at time t . Then, for each component i , the contribution coefficient is defined as:

$$C_i := \mathbb{E} \left[\frac{F_i}{\Phi} \right],$$

where Φ is a dominating function, i.e. $\Phi \geq |F_i|, \forall i$.

The total force, i.e. $\sum_i F_i$ excluding the inertial terms, is not a good candidate for a dominating function. Indeed, the terms often have opposite signs, and their sum can be really small. Another issue is given by the existence of a subset of times Θ characterized by the absence of flow in the selected location x . In Θ the dominant force is null, and cannot be the denominator of a fraction.

We explore two alternative Φ choices: Φ_1 is based on the l^1 norm, and defined as:

$$\Phi_1 := \begin{cases} \sum_i \frac{|F_i|}{2}, & \text{if not null;} \\ 1, & \text{otherwise.} \end{cases}$$

In case we exclude the inertial forces from the analysis, we must take $\hat{\Phi}_1 = 2\Phi_1$. In contrast Φ_2 is the dominant force, based on the l^∞ norm:

$$\Phi_2 := \begin{cases} \max_i |F_i|, & \text{if not null;} \\ 1, & \text{otherwise.} \end{cases}$$

In particular, for a particular location x , time t , and parameter sample η , we have $C_i = 0$ if there is no flow or all the forces are null. The expectation of C_i is reduced by the chance of F_i being small compared to the other terms, or by the chance of having no flow in (x, t) . Moreover, $\mathbb{E}[C_i] \in [-1, 1], \forall i$.

Proposition 2 Let $\Phi_k, k = 1, 2$ be the functions described above. Then they are well defined dominating function, i.e. $\Phi_k \geq |F_j|, \forall j, k$.

Proof. If $k = 1$, the Newton equation states $\sum_{j \in J} F_j = \sum_{i \in I} F_i$, where $(F_j)_{j \in J}$ are inertial forces, and $(F_i)_{i \in I}$ the local forces. Then, $\forall h \in I$

$$F_h = \sum_{i \neq h, i \in I} F_i - \sum_{j \in J} F_j.$$

And hence

$$|F_h| \leq |F_h| + \sum_{i \neq h, i \in I} |F_i| - \sum_{j \in J} |F_j| = 2\Phi_1.$$

A similar equation is valid $\forall k \in J$. If $k = 2$, or if the inertial forces are not included, the proof is trivial. \square

Furthermore, assuming $\Phi = \Phi_2$, there is a useful result explaining the meaning of those coefficients through the conditional expectation.

Proposition 3 Let $(F_i)_{i=1,\dots,n}$ be random variables on (Ω, \mathcal{F}, P) , representing the considered force components in location x at time t . For each i , let C_i be the contribution coefficient of force F_i , assuming $\Phi = \Phi_2$. Then we have the following expression:

$$C_i = \sum_j p_j \mathbb{E} \left[\frac{F_i}{|F_j|} \mid \Phi = |F_j| \right],$$

where $p_j := P\{\Phi = |F_j|\}$.

Proof. Let Z be a discrete random variable such that, for each $j \in \mathbb{N}$, $(Z = j) \iff (\Phi = |F_j|)$. Then, by the rule of chain expectation:

$$\begin{aligned} C_i &= \mathbb{E} \left[\frac{F_i}{\Phi} \right] = \mathbb{E} \left[\mathbb{E} \left[\frac{F_i}{\Phi} \mid Z = j \right] \right] = \\ &= \mathbb{E} \left[\mathbb{E} \left[\frac{F_i}{|F_j|} \mid Z = j \right] \right] = \sum_j P\{Z = j\} \mathbb{E} \left[\frac{F_i}{|F_j|} \mid Z = j \right]. \end{aligned}$$

Moreover, by definition, $p_j = P\{Z = j\}$. This completes the proof. \square

The last proposition brings to the definition of the dominance factors $(p_j)_{j=1,\dots,k}$, i.e. the probability of each F_j to be the dominant force in (x, t) .

Definition 4 (Dominance factors and conditional contributions) Let $(F_i)_{i=1,\dots,k}$ be random variables on (Ω, \mathcal{F}, P) , representing arbitrary force components in location x at time t . Then, for each pair of components (i, j) , the conditional contribution $C_{i,j}$ is defined as:

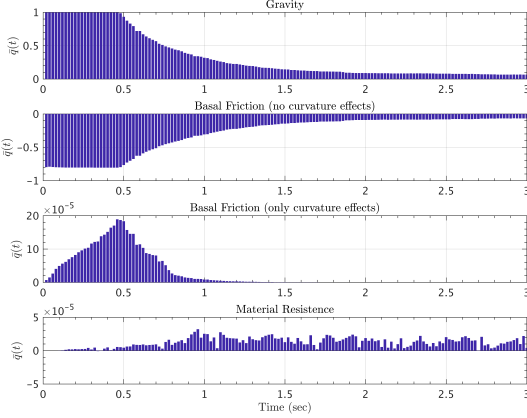
$$C_{i,j} := \mathbb{E} \left[\frac{F_i}{|F_j|} \mid \Phi = |F_j| \right],$$

where $\Phi = \Phi_2$ is the dominant force. In particular, for each component i , the dominance factor is defined as:

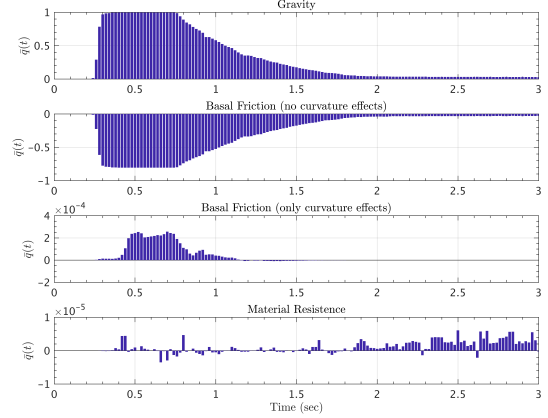
$$p_j := P \{ \Phi = |F_j| \}.$$

In the following we display the contribution coefficients barplots as a function of time, for the locations x_1, \dots, x_4 defined above. Moreover, we report the dominance factors plots, a very useful tool to read the dynamical significance of the forces as a function of time and location.

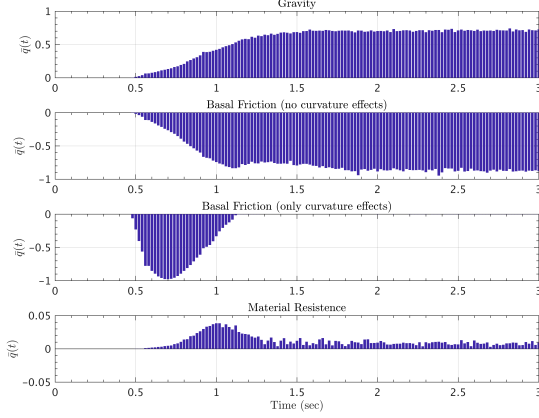
3.1.4 Mohr-Coulomb Model, Force Contribution Coefficients - Ali



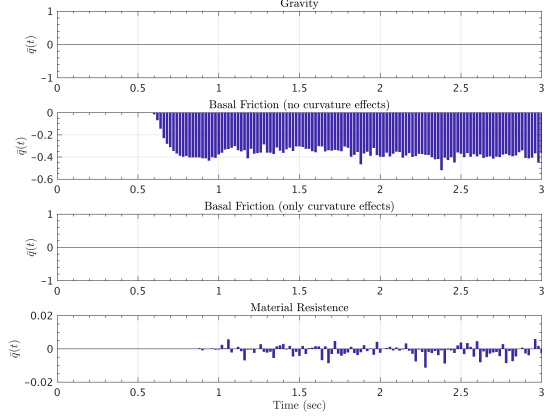
(a) $L_1 = (-0.7, 0)$, slumping pile location.



(b) $L_2 = (-0.35, 0)$, middle point on inclined plane.

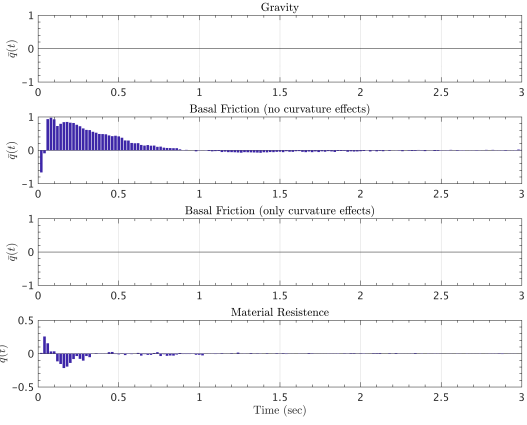


(c) $L_3 = (0, 0)$, inclined and runout planes' joint location.

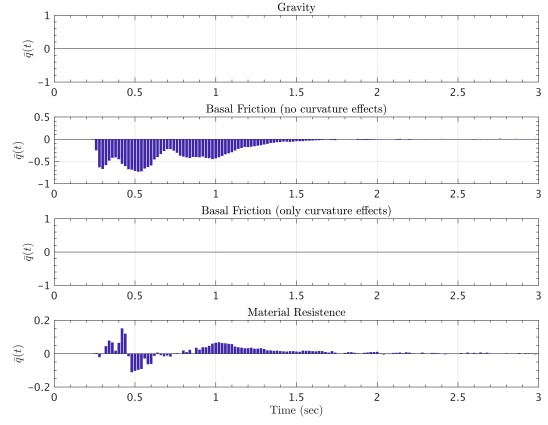


(d) $L_4 = (0.15, 0)$, a location on runout plane.

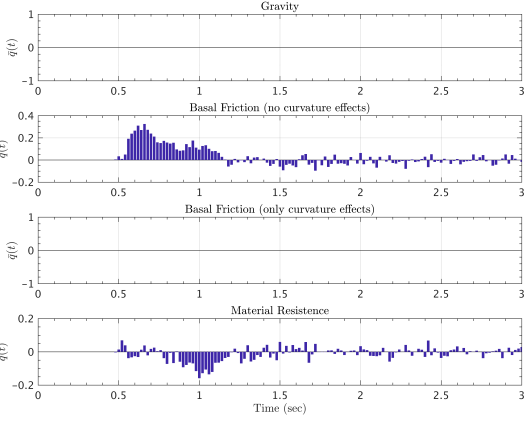
Figure 35: Time history of mean values for force impact quotients, $\bar{q}_i(t)$, along runout direction, Mohr-Coulomb model.



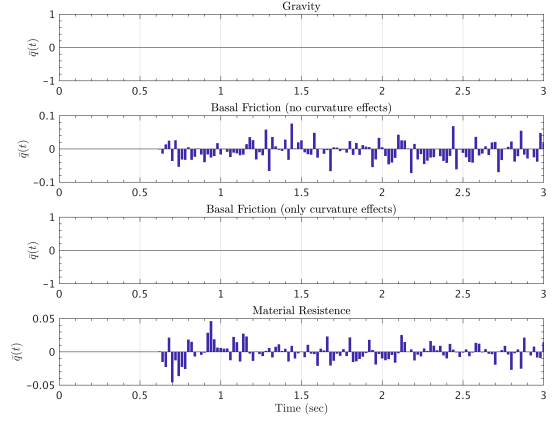
(a) $L_1 = (-0.7, 0)$, slumping pile location.



(b) $L_2 = (-0.35, 0)$, middle point on inclined plane.



(c) $L_3 = (0, 0)$, inclined and runout planes' joint location.



(d) $L_4 = (0.15, 0)$, a location on runout plane.

Figure 36: Time history of mean values for force impact quotients, $\bar{q}_i(t)$, along the lateral direction, Mohr-Coulomb model.

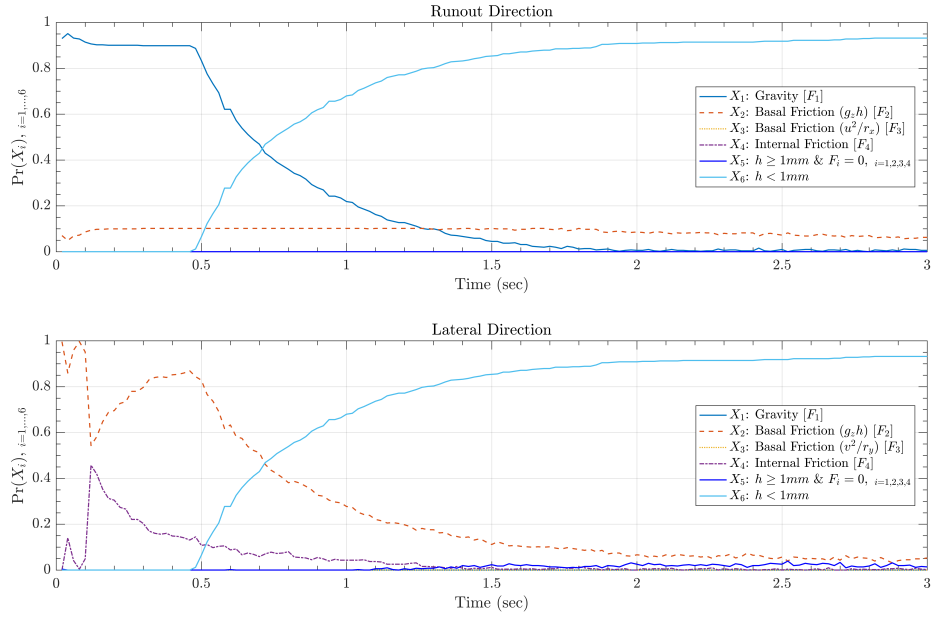


Figure 37: $L_1 = (-0.7, 0)$, slumping pile location.

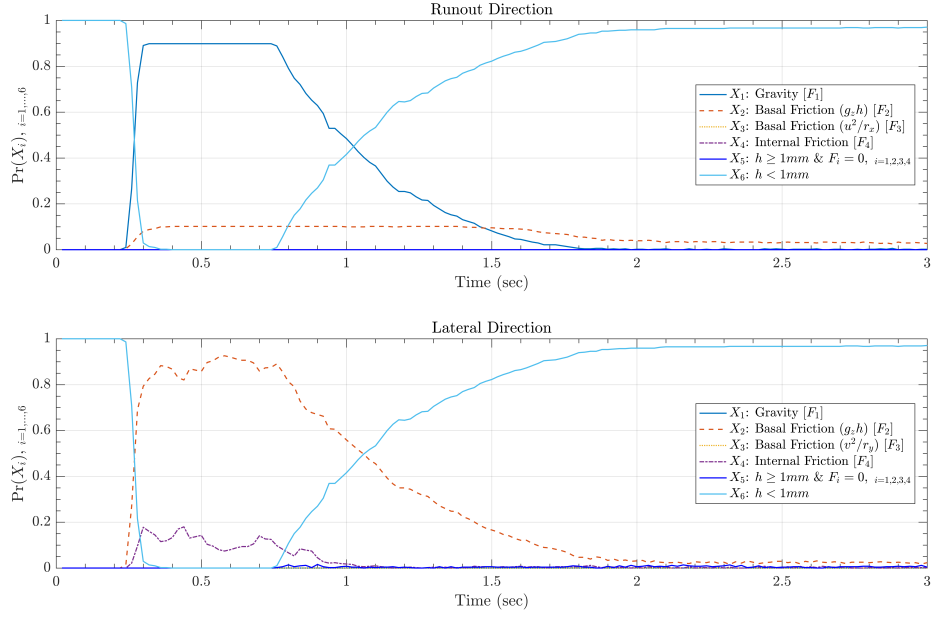


Figure 38: $L_2 = (-0.35, 0)$, middle point on inclined plane.

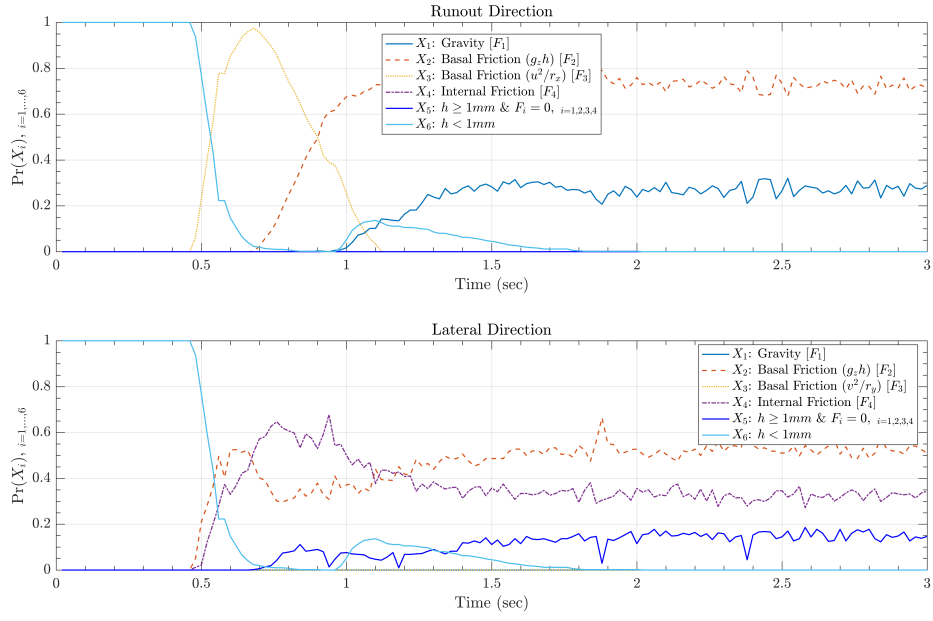


Figure 39: $L_3 = (0, 0)$, inclined and runout planes' joint location.

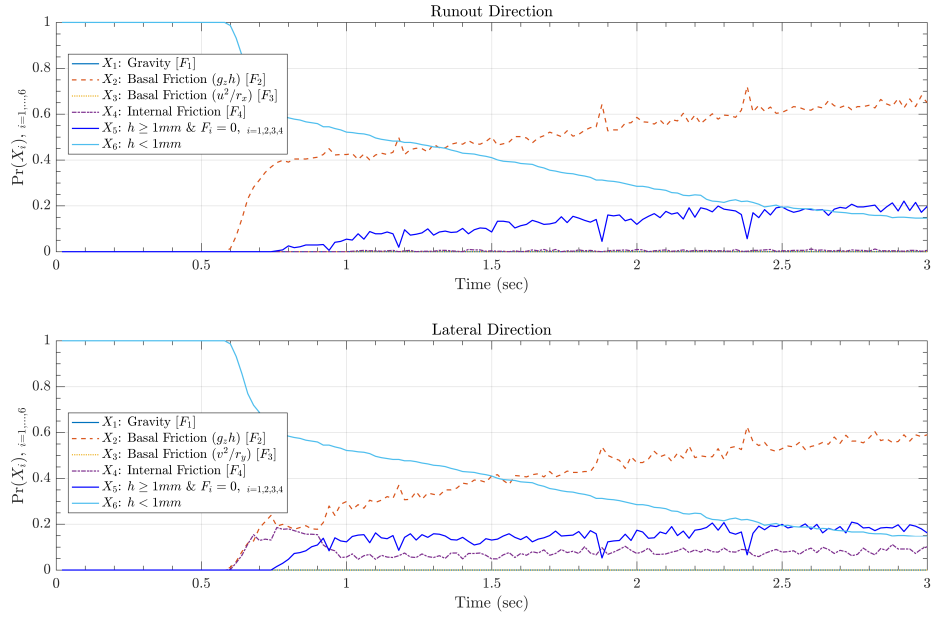
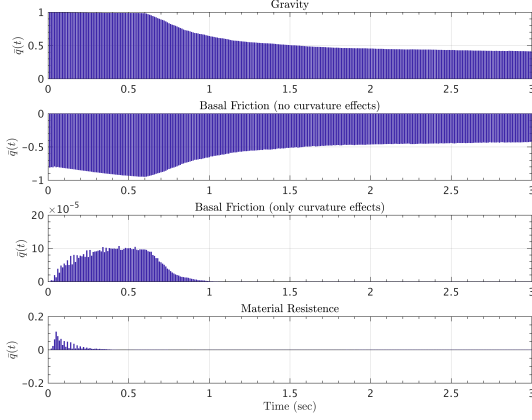
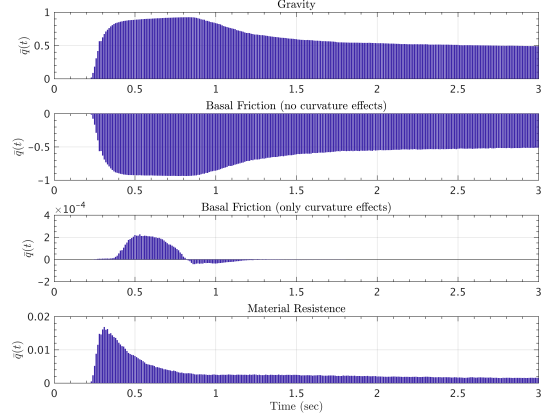


Figure 40: $L_4 = (0.15, 0)$, a location on runout plane.

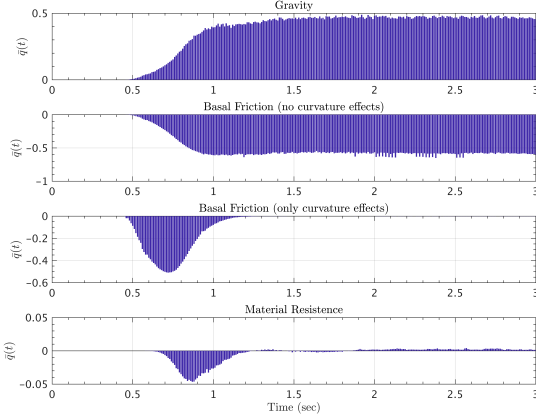
3.1.5 Pouliquen-Forterre Model, Force Contribution Coefficients - Ali



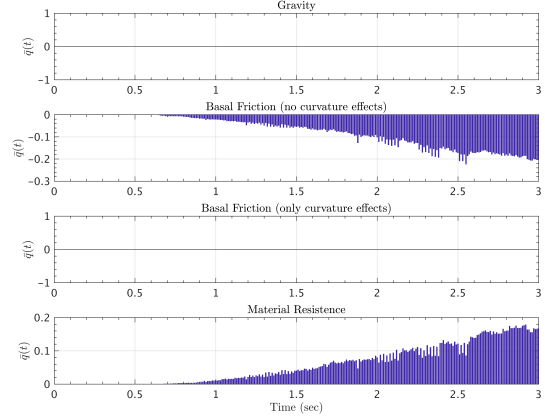
(a) $L_1 = (-0.7, 0)$, slumping pile location.



(b) $L_2 = (-0.35, 0)$, middle point on inclined plane.

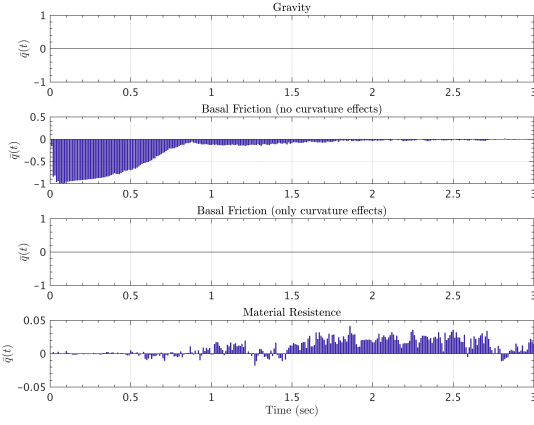


(c) $L_3 = (0, 0)$, inclined and runout planes' joint location.

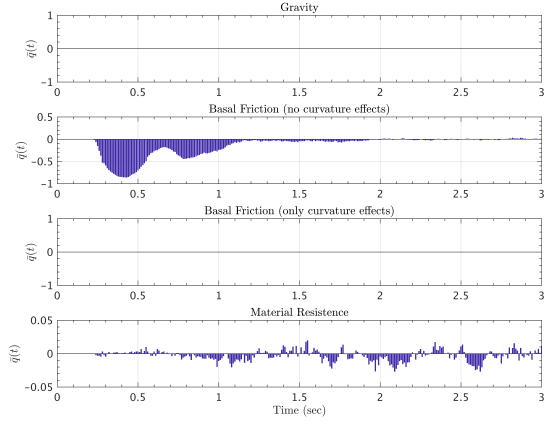


(d) $L_4 = (0.15, 0)$, a location on runout plane.

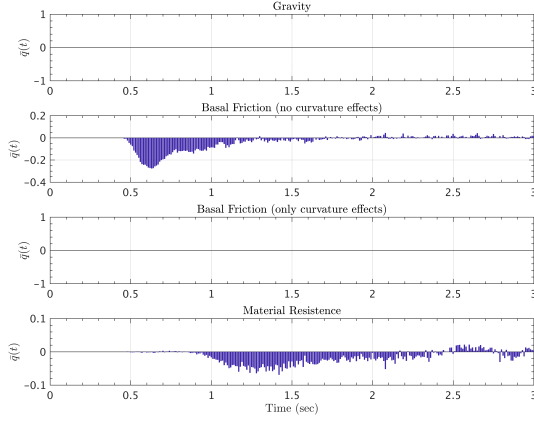
Figure 41: Time history of mean values for force impact quotients, $\bar{q}_i(t)$, along runout direction, Pouliquen-Forterre model.



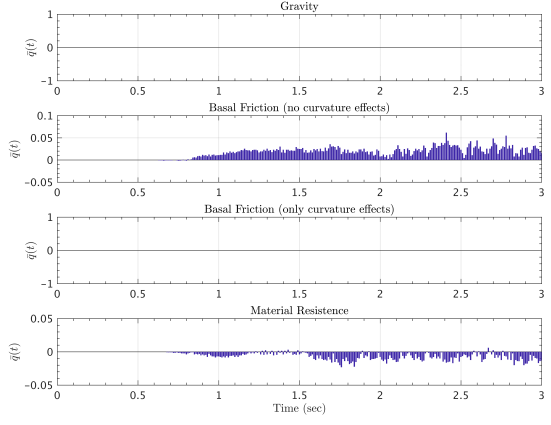
(a) $L_1 = (-0.7, 0)$, slumping pile location.



(b) $L_2 = (-0.35, 0)$, middle point on inclined plane.



(c) $L_3 = (0, 0)$, inclined and runout planes' joint location.



(d) $L_4 = (0.15, 0)$, a location on runout plane.

Figure 42: Time history of mean values for force impact quotients, $\bar{q}_i(t)$, along the lateral direction, Pouliquen-Forterre model.

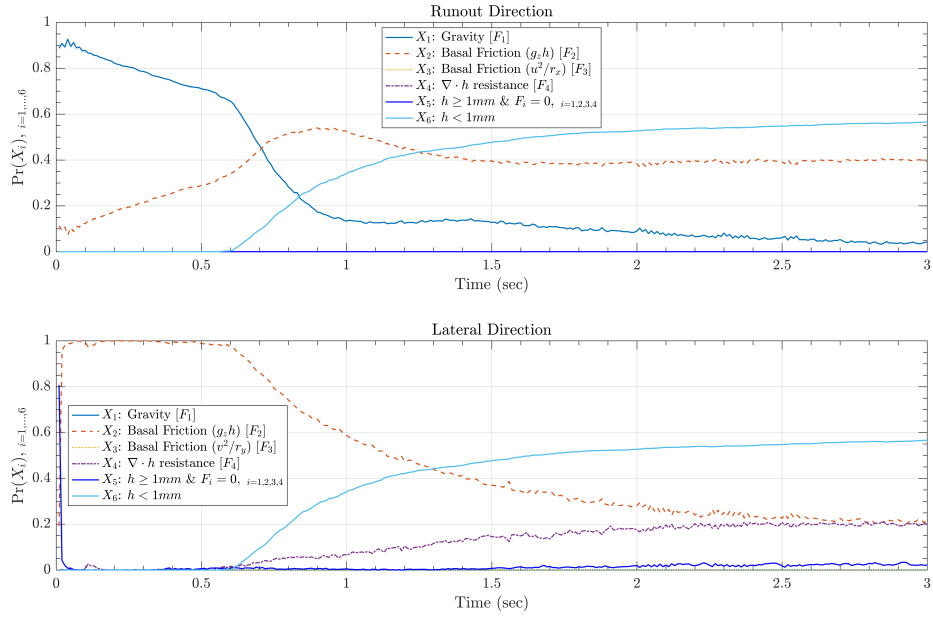


Figure 43: $L_1 = (-0.7, 0)$, slumping pile location.

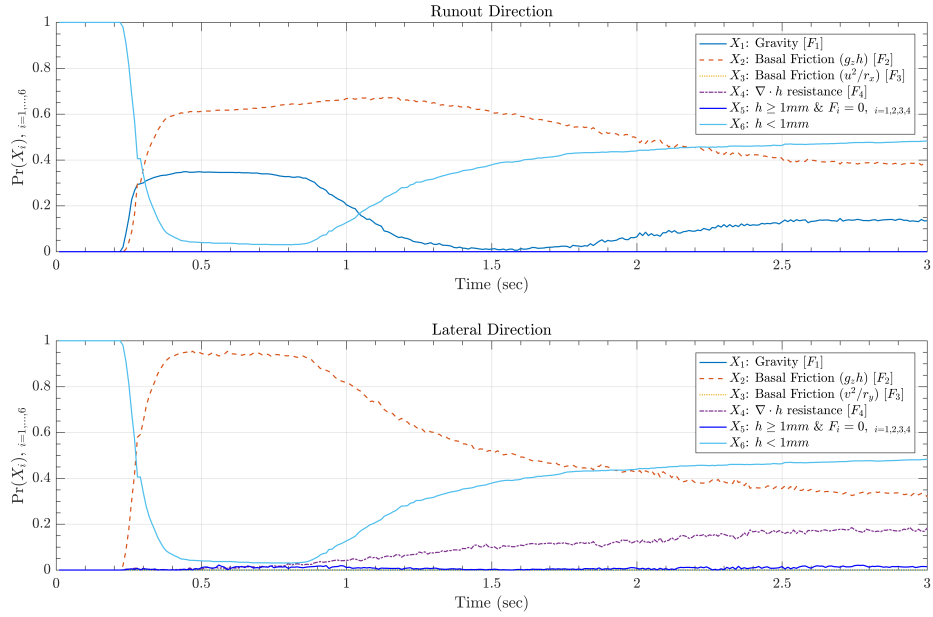


Figure 44: $L_2 = (-0.35, 0)$, middle point on inclined plane.

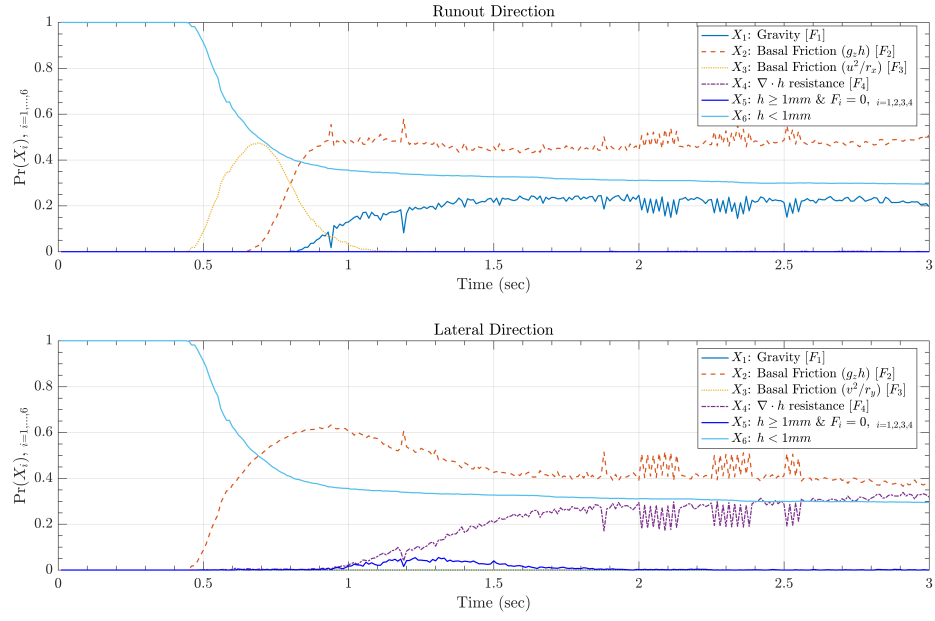


Figure 45: $L_3 = (0, 0)$, inclined and runout planes' joint location.

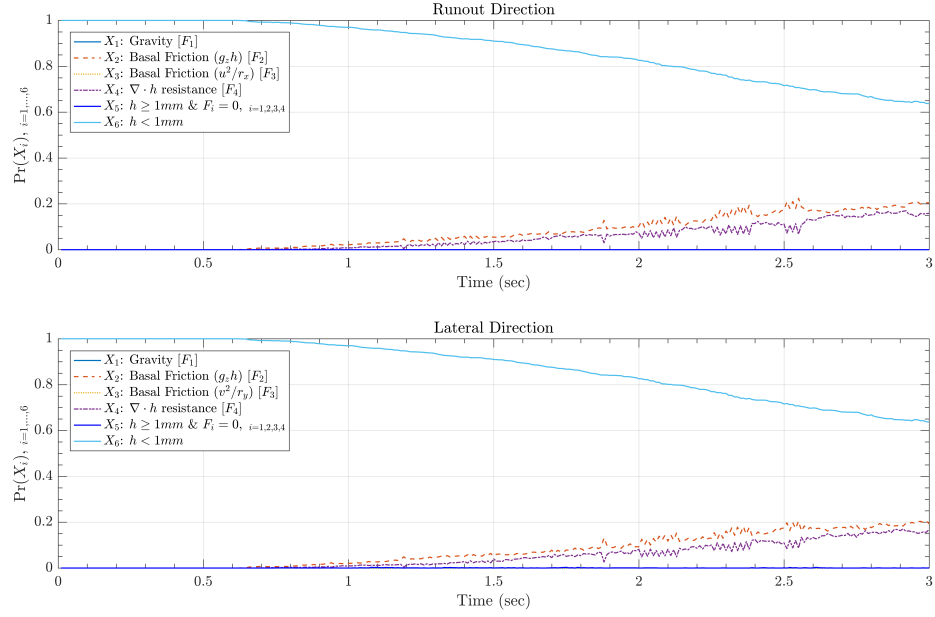
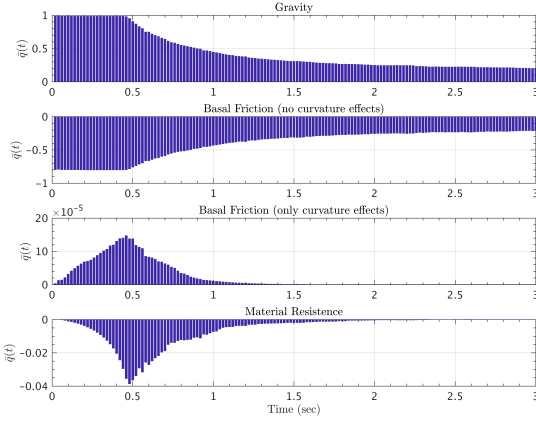
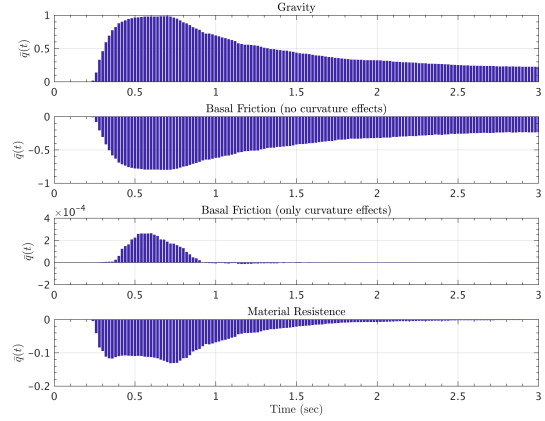


Figure 46: $L_4 = (0.15, 0)$, a location on runout plane.

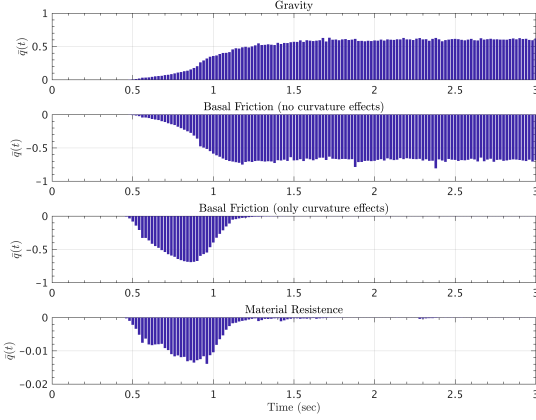
3.1.6 Voellmy-Salm Model, Force Contribution Coefficients - Ali



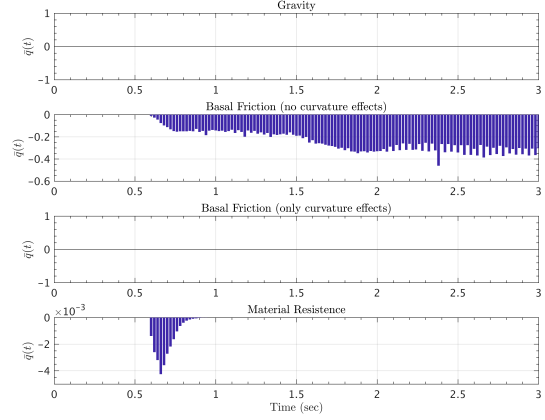
(a) $L_1 = (-0.7, 0)$, slumping pile location.



(b) $L_2 = (-0.35, 0)$, middle point on inclined plane.

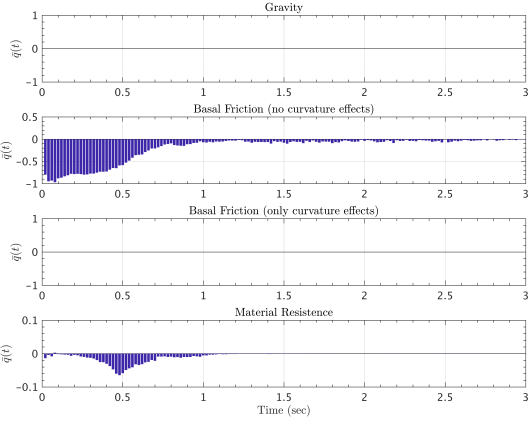


(c) $L_3 = (0, 0)$, inclined and runout planes' joint location.

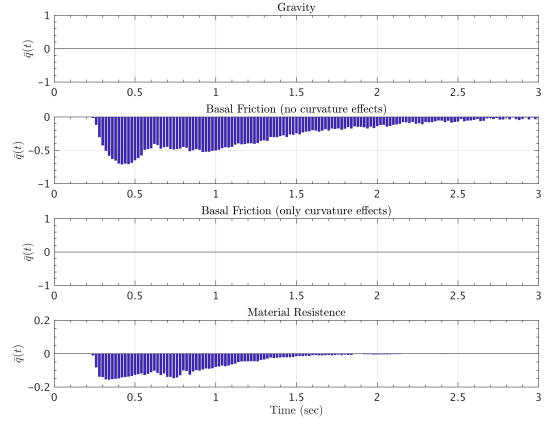


(d) $L_4 = (0.15, 0)$, a location on runout plane.

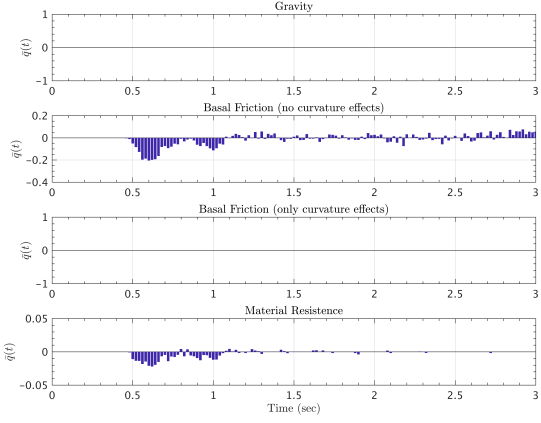
Figure 47: Time history of mean values for force impact quotients, $\bar{q}_i(t)$, along runout direction, Voellmy-Salm model.



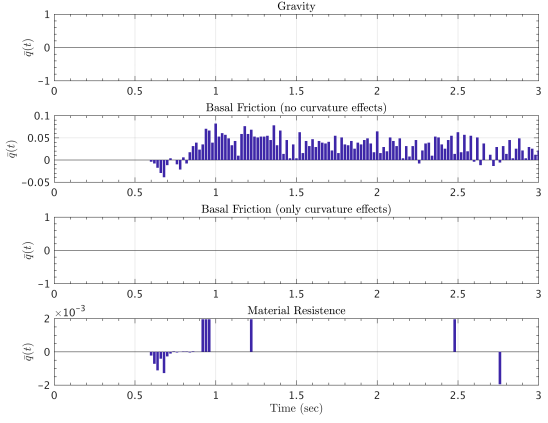
(a) $L_1 = (-0.7, 0)$, slumping pile location.



(b) $L_2 = (-0.35, 0)$, middle point on inclined plane.



(c) $L_3 = (0, 0)$, inclined and runout planes' joint location.



(d) $L_4 = (0.15, 0)$, a location on runout plane.

Figure 48: Time history of mean values for force impact quotients, $\bar{q}_i(t)$, along the lateral direction, Voellmy-Salm model.

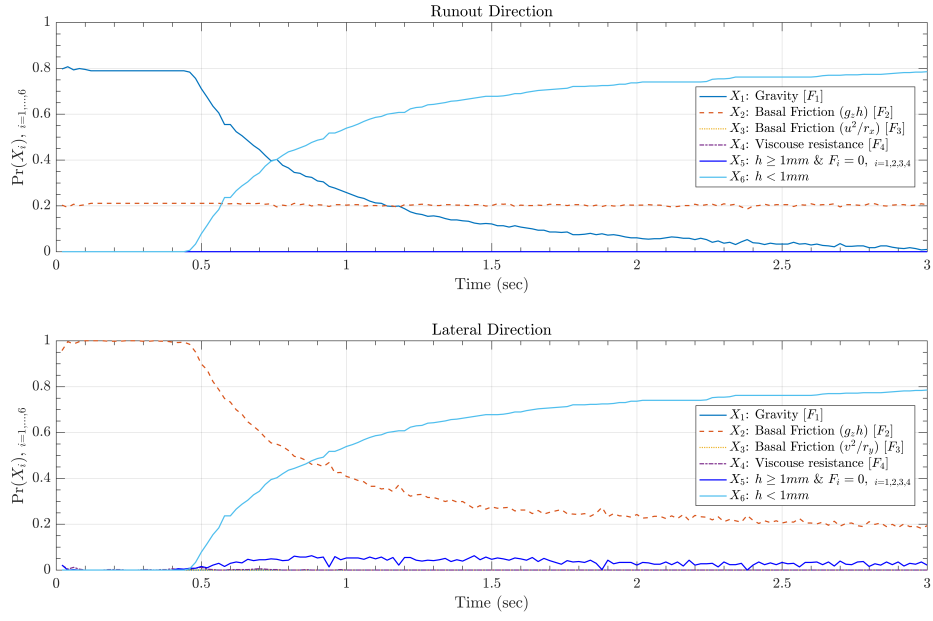


Figure 49: $L_1 = (-0.7, 0)$, slumping pile location.

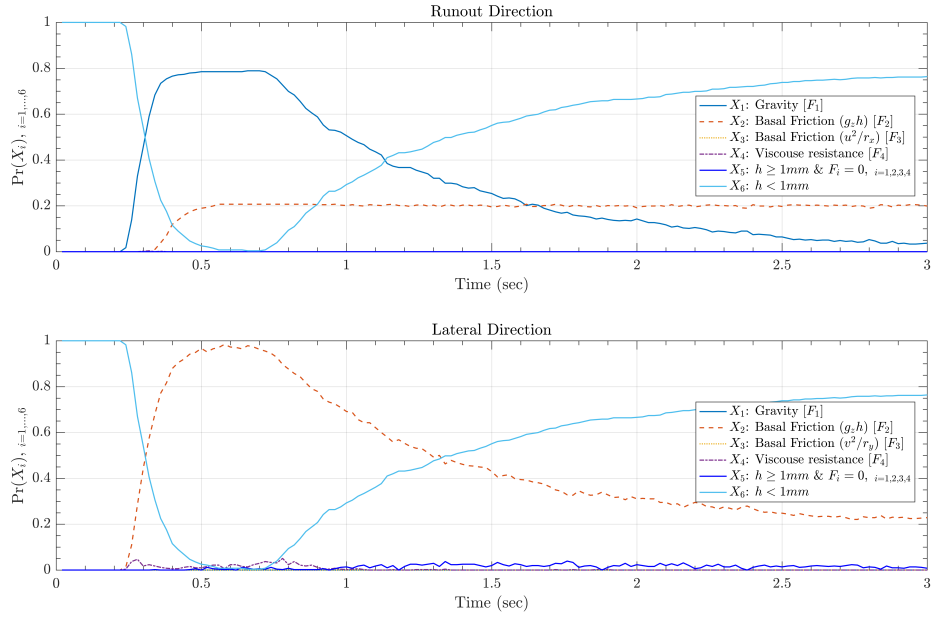


Figure 50: $L_2 = (-0.35, 0)$, middle point on inclined plane.

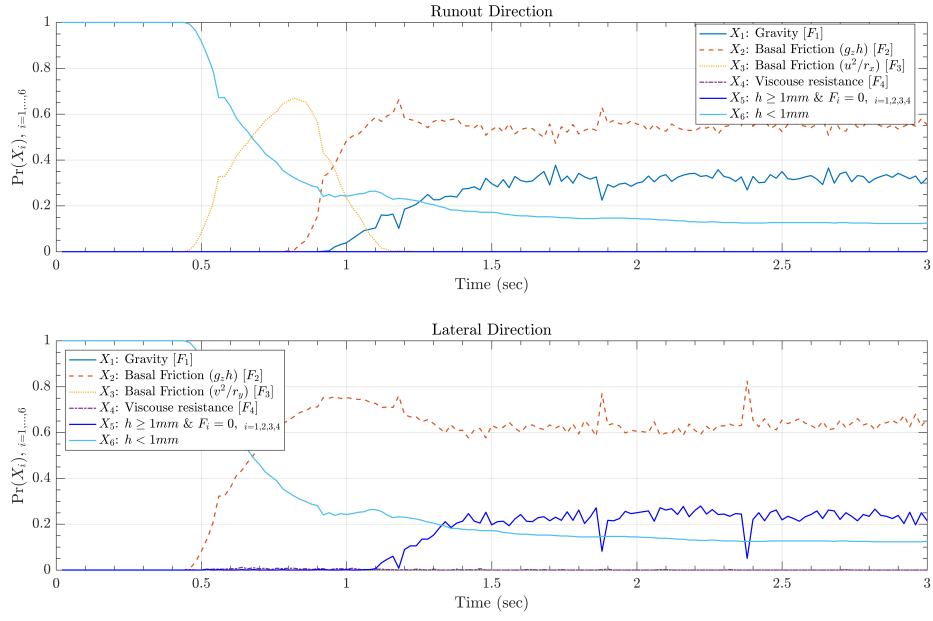


Figure 51: $L_3 = (0, 0)$, inclined and runout planes' joint location.

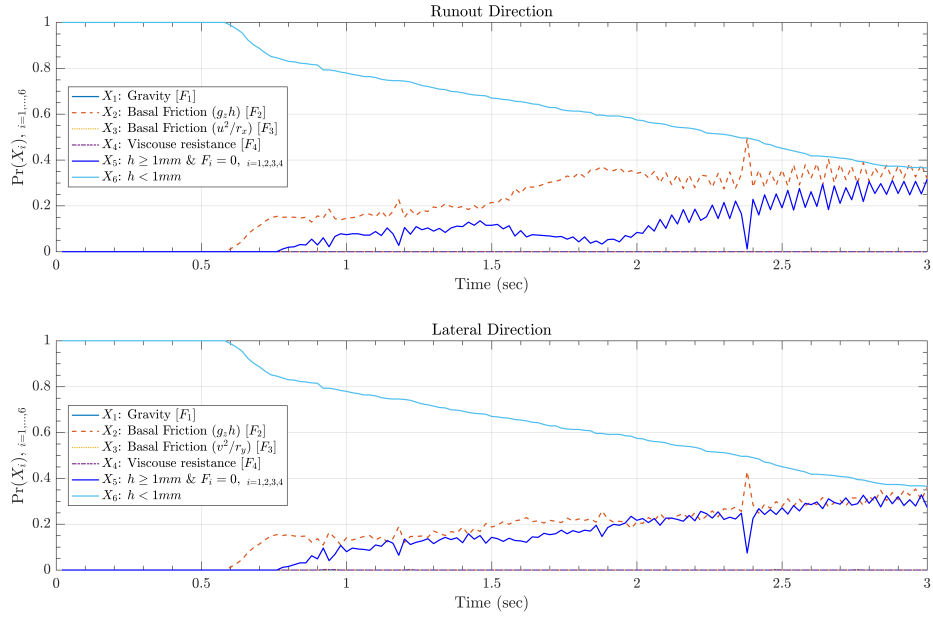


Figure 52: $L_4 = (0.15, 0)$, a location on runout plane.

4 Results and Discussion – All

Appendix A: Latin Hypercubes and orthogonal arrays - Andrea

The Latin Hypercube Sampling (LHS) is a well established procedure for defining pseudo-random designs of samples in \mathbb{R}^d , with good properties with respect to the uniform probability distribution on an hypercube $[0, 1]^d$ (McKay et al., 1979; Stein, 1987; Ranjan and Spencer, 2014; Ai et al., 2016). In particular, compared to a random sampling, a LHS: (i) enhances the capability to fill the d-dimensional space with a finite number of points, (ii) in case $d > 1$, avoids the overlapping of point locations in the one dimensional projections, (iii) reduces the dependence of the number of points necessary on the dimensionality d .

Definition 5 (Latin hypercube sampling) Let $\Xi = \{\xi_i : i = 1, \dots, N\}$ be a set of points inside the d -dimensional hypercube $C = [0, 1]^d$. Let $[0, 1] = \bigcup_{j=1}^N I_j$, where $I_j = [\frac{(j-1)}{N}, \frac{j}{N}]$. Let $\xi_i = (\xi_i^1, \dots, \xi_i^d)$, and for each $k \in \{1, \dots, d\}$, let $\Xi^k = \{\xi_i^k : i = 1, \dots, N\}$. Let λ^d be the uniform probability measure supported inside C , called Lebesgue measure. Then Ξ is a latin hypercube w.r.t. $\lambda^d \iff \forall j \in \{1, \dots, N\}, \forall k \in \{1, \dots, d\}, |I_j \cap \Xi^k| = 1$.

The procedure is simple: once the desired number of samples $N \in \mathbb{N}$ is selected, and $[0, 1]$ is divided in N equal bins, then each bin will contain one and only one projection of the samples over every coordinate. The LHS definition is trivially generalized over $C = \prod_i^d [a_i, b_i]$, i.e. the cartesian product of d arbitrary intervals. That will be applied in this study, defining LHS over the parameter domain of the flow models.

There are a large number of possible designs, corresponding the number of permutations of the bins in the d -projections, i.e. $d \cdot N!$. If the permutations are randomly sampled there is a high possibility that the design will have good properties. However, this is not assured, and clusters of points or regions of void space may be observed in C . For this reason, we base our design on the orthogonal arrays (OA) (Owen, 1992; Tang, 1993).

Definition 6 (Orthogonal arrays) Let $S = \{1, \dots, s\}$, where $s \geq 2$. Let $Q \in S^{n \times m}$ be a matrix of such integer values. Then Q is called an $OA(n, m, s, r) \iff$ each $n \times r$ submatrix of Q contains all possible $1 \times r$ row vectors with the same frequency $\lambda = n/s^r$, which is called the index of the array. In particular, r is called the strength, n the size, ($m \geq r$) the constraints, and s the levels of the array.

Orthogonal arrays are very useful for defining latin hypercubes which are also forced to fill the space (or its r -dimensional subspaces) in a more robust way, at the cost of potentially requiring a larger number of points than a traditional LHS.

Proposition 7 Let Q be an $OA(n, m, s, r)$. Then let $U \in \mathbb{R}^{n \times m}$ be defined as follows:

$$\forall k \in \{1, \dots, s\}, \forall j \in \{1, \dots, m\}, \{Q[\cdot, j] : Q[i, j] = k\} = \Pi(\{(k-1)\lambda s^{r-1}, \dots, k\lambda s^{r-1}\}),$$

where Π is a random permutation of λs^{r-1} elements. Then $\Xi = \{\xi_i = U[i, \cdot] : i = 1, \dots, n\}$ is a LHS w.r.t to λ^m over $C = [0, 1]^m$. Moreover, let $[0, 1]^r = \bigcup_{(h_1, \dots, h_r)=1}^s I_{(h_i)}$, where $I_{(h_i)} = \prod_i^r [\frac{(h_i-1)}{s}, \frac{h_i}{s}]$. Then $\forall D = (d_1, \dots, d_r) \subseteq \{1, \dots, m\}$, let $\Xi^D = \{(\xi^{d_1}, \dots, \xi^{d_r}) : i = 1, \dots, n\}$. We have that

$$\forall k \in \{1, \dots, s\}, \forall (h_i : i = 1, \dots, r) \in \{1, \dots, d\}^r, |I_{(h_i)} \cap \Xi^D| = \lambda.$$

For each column of Q we are replacing the λs^{r-1} elements with entry k by a random permutation of $((k-1)\lambda s^{r-1} + h)_{h \in \{1, \dots, \lambda s^{r-1}\}}$. After the replacement procedure is done, the newly obtained matrix U is equivalent to a LHS which inherits from Q the property of fully covering s^r equal r -dimensional hypercubes in every r -dimensional projection. Each hypercube contains λ points. In other words, inside each r -dimensional projection, the design associated to U fills the space like a regular grid at the scale of those s^r hypercubes, but it is still an LHS at a finer scale, i.e. the λs^{r-1} one dimensional bins. A complete proof can be found in Tang (1993) and it is a straightforward verification of the required properties.

However, even in an LHS based on an $OA(n, m, s, r)$, if $r < m$ what happens in the projections with dimension $r' > r$ is not controlled, and randomizing procedures are made more difficult by the additional structure imposed by the OA. Moreover, the total number of points necessary to achieve a full design increases with r , and hence is affected by dimensionality issues.

Dealing with relatively small d , i.e. $d \in \{3, 4\}$, we adopt a LHS U created by a $OA(s^d, d, s, d)$. The strength is equal to the dimension d , hence the design fills the entire space like a d dimensional grid, but it is a LHS as well. In this case there is one point in each hypercube, and $\lambda = 1$. We take $s = 8$ for the 3-dimensional designs over the parameter space of Mohr-Coulomb and Voellmy-Salm models, i.e. 512 points; we took $s = 6$ for the 4-dimensional designs over the more complex parameter space of the Pouliquen-Forterre model, i.e. 1296 points.

References

- Ai, M., Kong, X., and Li, K. (2016). A general theory for orthogonal array based latin hypercube sampling. *Statistica Sinica*, (26):761–777.
- Barker, T., Schaeffer, D. G., Bohorquez, P., and Gray, J. M. N. T. (2015). Well-posed and ill-posed behaviour of the $\mu(i)$ -rheology for granular flow. *Journal of Fluid Mechanics*, 779:794–818.
- Bartelt, P., Salm, B., and Gruber, U. (1999). Calculating dense-snow avalanche runout using a voellmy-fluid model with active/passive longitudinal straining. *Journal of Glaciology*, 45(150):242–254.
- Dalbey, K., Patra, A. K., Pitman, E. B., Bursik, M. I., and Sheridan, M. F. (2008). Input uncertainty propagation methods and hazard mapping of geophysical mass flows. *Journal of Geophysical Research: Solid Earth*, 113:1–16.
- Denlinger, R. P. and Iverson, R. M. (2001). Flow of variably fluidized granular masses across three-dimensional terrain: 2. Numerical predictions and experimental tests. *Journal of Geophysical Research*, 106(B1):553–566.
- Forsterre, Y. and Pouliquen, O. (2003). Long-surface-wave instability in dense granular flows. *Journal of Fluid Mechanics*, 486:21–50.
- Freundt, A. and Bursik, M. I. (1998). Pyroclastic flow transport mechanisms. In Freundt, A. and Rosi, M., editors, *From Magma to Tephra: Modelling Physical Processes of Explosive Volcanism*, volume 4 of *Advances in Volcanology*, pages 151–222. Elsevier Science, Amsterdam.
- Gray, J. M. N. T. and Edwards, A. N. (2014). A depth-averaged $\mu(I)$ -rheology for shallow granular free-surface flows. *Journal of Fluid Mechanics*, 755:503–534.
- Hutter, K., Siegel, M., Savage, S. B., and Nohguchi, Y. (1993). Two-dimensional spreading of a granular avalanche down an inclined plane part I. Theory. *Acta Mechanica*, 100:37–68.
- Iverson, R. M. and Denlinger, R. P. (2001). Flow of variably fluidized granular masses across three-dimensional terrain: 1. Coulomb mixture theory. *Journal of Geophysical Research*, 106(B1):537.
- McKay, M. D., Beckman, R. J., and Conover, W. J. (1979). A comparison of three methods for selecting values of input variables in the analysis of output from a computer code. *Technometrics*, 21(2):239–245.
- Owen, A. B. (1992). Orthogonal arrays for computer experiments, integration and visualization. *Statistica Sinica*, 2(2):439–452.
- Pudasaini, S. and Hutter, K. (2007). *Avalanche Dynamics: Dynamics of Rapid Flows of Dense Granular Avalanches*. Springer.
- Ranjan, P. and Spencer, N. (2014). Space-filling latin hypercube designs based on randomization restrictions in factorial experiments. *Statistics and Probability Letters*, 94(Supplement C):239 – 247.
- Savage, S. B. and Hutter, K. (1989). The motion of a finite mass of granular material down a rough incline. *Journal of Fluid Mechanics*, 199:177.
- Stein, M. (1987). Large sample properties of simulations using latin hypercube sampling. *Technometrics*, 29(2):143–151.
- Tang, B. (1993). Orthogonal array-based latin hypercubes. *Journal of the American Statistical Association*, 88(424):1392–1397.